ACS Catalysis

pubs.acs.org/acscatalysis
Research Article

Microkinetic Modeling of Support Effects in PdO-Based Methane Oxidation Catalysts

Rinu Chacko,[#] Kevin Keller,[#] Akash B. Shirsath, Sofia Angeli, Patrick Lott, and Olaf Deutschmann*

Cite This: ACS Catal. 2025, 15, 6937−6952
Read Online

ACCESS | Metrics & More | Article Recommendations | Supporting Information

ABSTRACT: The impact of different support materials on the catalytic activity of PdO-based catalysts during methane oxidation is studied using microkinetic modeling. Two independent sets of microkinetic data were developed, numerically studied, and validated with experimental data obtained in dry and various humid reaction gas mixtures. An automated optimization routine refined the original physics-based mechanism, resulting in a set of thermodynamically consistent kinetic parameters for PdO/SnO_2 and PdO/ZrO_2 that accurately describe the catalytic measurements. The findings indicate that SnO_2 and ZrO_2 supports enhance catalytic activity and methane conversion, even in the presence of water. Despite potential inhibition from hydroxyl formation on the catalyst surface, the results of the kinetic models show a significant influence of the support materials on the reactions occurring on the PdO surface. Sensitivity analyses of the refined mechanisms identify essential kinetic parameters and reaction pathways of the developed mechanisms under dry and humid conditions. Overall, this study illustrates the effectiveness of the automated optimization approach in accelerating kinetic model development and incorporating reaction engineering over different supports, which may be exploited for scale-up processes.

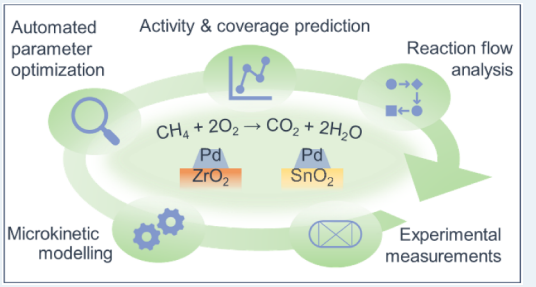

KEYWORDS: *emission control, methane oxidation, microkinetic modeling, PdO catalyst, model optimization*

INTRODUCTION

Despite decades of scientific efforts for finding more suitable materials, catalysts based on palladium (Pd), most frequently supported on alumina (Al_2O_3),[1,2] remain the premier choice for total oxidation of methane (CH_4) in the low temperature regime under lean conditions. These Pd/Al_2O_3 catalysts typically exhibit a high initial activity for activating the CH_4 molecule with its symmetric molecular structure and stable C−H bonds.[3,4] However, severe inhibition occurs in the presence of water (H_2O),[5−9] and pronounced deactivation has been reported during long-term operation under humid conditions.[7,8,10,11] Since the efficient removal of the strong greenhouse gas methane[12] is of utmost importance for modern exhaust gas after treatment systems of natural gas engines[13,14] and in general methane emissions occurring in the chemical industry or in the energy production sector, concepts are necessary that allow to overcome both inhibition and long-term deactivation. Beyond the addition of Pt to Pd-based catalysts, which has been reported to be beneficial with regard to catalytic activity, resilience toward water, and sintering prevention,[15−17] the support material also offers chances to optimize the catalytic activity and stability. Although a variety of studies have addressed support modifications,[18−21] the exact role of the support material during Pd-catalyzed CH_4 conversion remains poorly understood. Aspects such as the highly dynamic Pd−PdO transformation of the noble metal phase that takes place under reactive conditions and becomes particularly relevant during dynamic catalyst operation,[22] and the fact that CH_4 oxidation depends on the noble metal particle size,[23,24] add to the complexity of such noble metal−support interactions.

Catalyst deactivation is primarily attributed to hydroxyl formation and subsequent blockage of active sites,[9,25,26] originating either from hydroxylation of PdO by H_2O from the gas phase or directly from surface H_2O intermediates as a consequence of the surface oxidation reactions.[27,28] Hydroxyl accumulation on the support material has been observed as well.[25,29] Previous studies pointed out that supports with higher oxygen mobility[30−32] such as ceria and zirconia[26] may be able to mitigate the negative effect of OH species, which are supposed to impact the catalytic methane oxidation activity.[31] Additionally, surface reoxidation of the noble metal particles PdO crucially influences the catalytic activity.[33−36] Capturing all these effects either experimentally or by means of kinetic simulations is challenging, since a multitude of phenomena may take place simultaneously, which calls for a deconvolution. Although global kinetic models have been often described in

Received: January 20, 2025
Revised: March 25, 2025
Accepted: March 25, 2025
Published: April 14, 2025

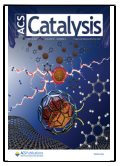

https://doi.org/10.1021/acscatal.5c00516
ACS Catal. 2025, 15, 6937−6952

the literature[19,37−40] and were demonstrated to simulate experimental data fairly well,[19,39,40] their application is frequently limited to the specific reactor environment that was used during the experimental measurements. Therefore, global kinetics that have not been designed for generalization do not allow for a comprehensive understanding of the underlying mechanism and impede direct knowledge transfer from simulations to optimization of the catalyst system. In contrast, the establishment of microkinetic models is less straightforward, since a great variety of reactions taking place on the surface of the catalyst need to be taken into account. Once validated, microkinetics offer great opportunities to study the catalyst at various conditions, since the model typically comprises all possible surface reactions and species.[41]

For the total oxidation of methane over PdO, which is assumed to be the predominant active species under lean conditions, a detailed mechanism has already been proposed and tested in different reaction environments.[9,42,43] DFT-based microkinetic models, however, may inherently contain uncertainties of up to 30 kJ mol^{-1} in the calculated energy barriers.[44−46] For complex systems such as methane oxidation, these uncertainties can build up to considerable extent[47,48] and may even change the rate-determining step.[49] As described by Kreitz et al.,[48,50] the DFT-related error propagation can be investigated during mechanism development with the Reaction Mechanism Generator (RMG),[51] which uncovers the effects of this restriction during reactor simulations. To this point, the approach for mean-field microkinetic models is considering the given reactions attributed to the active surface of the catalyst, namely, PdO. Herein, no participation of the support material on the catalytic reaction network is considered. However, the support material of the catalyst influences the catalytic performance,[20,52−54] which particularly highlights the need for tailored mechanisms for different catalyst formulations. In the context of CH_4 oxidation, the use of SnO_2 as a support material has been reported to enable a well-balanced interaction between the noble metal and the support, which is assumed to enhance the water resilience.[6,55,56] In particular, SnO_2 may not only assist in the activation of oxygen,[57] which could benefit the methane oxidation rate in the presence of water, but may also contribute to high catalytic activity due to its reducibility that contributes to the redox behavior of the active palladium species.[19,55] Furthermore, compared to Al_2O_3, SnO_2 is assumed to facilitate dehydroxylation,[58] possibly influenced by H_2O adsorption enthalpies on PdO that vary for SnO_2- and Al_2O_3-supported catalysts.[6] As an alternative, ZrO_2 as a support material might help sustain a good reducibility of PdO particles on the surface of the catalyst due to improved metal−support interactions.[53] For this reason ZrO_2 is sometimes favored for methane oxidation catalysts as it influences the PdO/Pd stability and reducibility in dry conditions as well as in the presence of water,[19,59] combined with excellent hydrothermal stability,[8] compared to inert (SiO_2) or acidic (Al_2O_3) materials.[60]

Our recent work[61] demonstrated the suitability of the Basin-Hopping algorithm for optimizing the kinetic parameters of detailed surface reaction mechanisms while maintaining thermodynamic consistency. The use of automation in the generation of simulation input files, e.g., altering the kinetic model used within the simulation, and multiple parallelized execution calls at each iteration of the optimization routine enabled significant acceleration in finding the optimal solution, which is otherwise done manually. This approach is used for the total oxidation of methane over palladium-based catalysts with different support materials, namely SnO_2 and ZrO_2, in lean operation. First, it is described where discrepancies between existing models and experimental results originate from. Second, two sets of kinetic parameters of a multistep reaction mechanism are derived from the two kinds of catalysts using the results of experimental activity tests for these catalysts. Ultimately, differences in the reaction pathways and sensitivities of the parameters for all of the support materials studied are discussed using these two sets of reaction kinetic parameters.

METHODS

Kinetic Parameter Optimization Approach. The two reaction kinetic data sets for methane oxidation over PdO supported on SnO_2 and ZrO_2, respectively, are obtained using an automated reaction mechanism optimization procedure[61] as illustrated in Figure 1, leveraging existing physics-based models

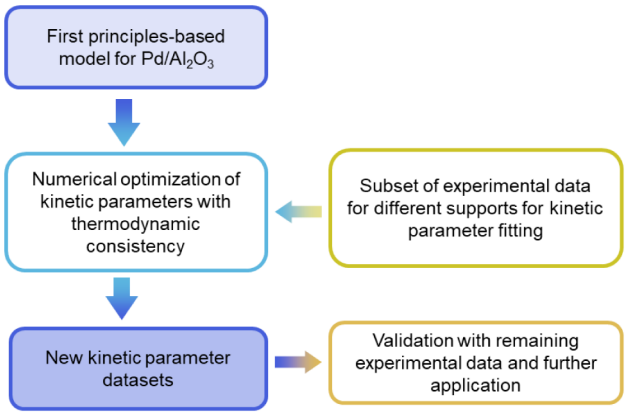

Figure 1. Graphical illustration of the optimization and validation process.

and experimental data under various operating conditions. A detailed surface reaction mechanism with first-principles-based reaction rate parameters[42] for a well-understood catalytic system, i.e., PdO/Al_2O_3 serves as a basis, as initial guesses to the kinetic parameters. Here, new kinetic parameters are obtained for PdO on different supports but with the same surface reactions by optimizing the parameters to match the catalytic performance on a subset of experimental data. This method accelerates model development for catalytic systems with existing detailed models, provided that the catalyst modification, here, the use of different supports, does not alter the underlying reaction mechanism. This approach can significantly speed up model development and support reaction engineering, as well as scale-up processes. Typically, technical catalyst development focuses on a single active material, improving its activity by varying supports and synthesis methods without changing the overall mechanism, highlighting a potential use case of the presented optimization approach.

The experimental performance data are utilized in part for the optimization process and in part for the validation procedure. The overall optimal set of new kinetic parameters was obtained by minimizing the error between the modeled and experimental methane conversion data, however, only for two conditions: 0 vol % H_2O (dry) and 1 vol % H_2O. In these sets only T_{10}, T_{50}, and T_{90}, i.e., the temperature of 10%, 50%,

https://doi.org/10.1021/acscatal.5c00516
ACS Catal. 2025, 15, 6937−6952

and 90% conversion, respectively, were chosen for the optimization routine. These conditions were chosen to minimize computational effort during the calculation of the objective function and to use the rest of the data to test the generalizability of the optimized models. Under these conditions, packed bed reactor simulations were performed at each iteration of the optimization routine, and the simulated data were compared with the experimental data to determine if the current set of kinetic parameters is accepted or not. Once the optimization procedure is complete and a new and optimized kinetic parameter set is obtained, the rest of the experimental data, which involve all humid concentrations between 2 and 12 vol % H_2O, were used for validation. Further details about the optimization procedure, the modeling details, and the characterization data used in simulations are provided in the Supporting Information.

RESULTS AND DISCUSSION

Methane Oxidation over SnO_2-Supported PdO Catalysts. As already outlined in the Introduction, lean-operated Pd-based methane oxidation catalysts greatly suffer from inhibition due to the presence of water, which is an inevitable component of the exhaust gas and is also formed during the reaction on the surface of the catalyst. As underscored by the experimental data depicted in Figure 2 (dots), the addition of only 1 vol % H_2O to the reaction gas mixture (3200 ppm of CH_4, 10 vol % O_2, and balance N_2) shifts the catalytic activity of the PdO/SnO_2 powder catalyst toward higher temperatures. A further increase in the steam concentration results in an increasing inhibition. In particular, T_{50}, the temperature at 50% conversion, is 588 K in a dry reaction gas mixture but rises to 675 K in the presence of 12 vol % H_2O. Such effects can be captured by mean-field microkinetic models that describe surface reactions taking place on the noble metal particles. For methane oxidation over PdO, Stotz et al.[42] published a mechanism based on DFT calculations.[43] In their study, activity tests focused on alumina-supported catalysts, highlighting how a blockage of active surface sites occurs by hydroxylation. This hydroxyl accumulation on both the noble metal and the support material is the primary origin of water inhibition and long-term deactivation.[9]

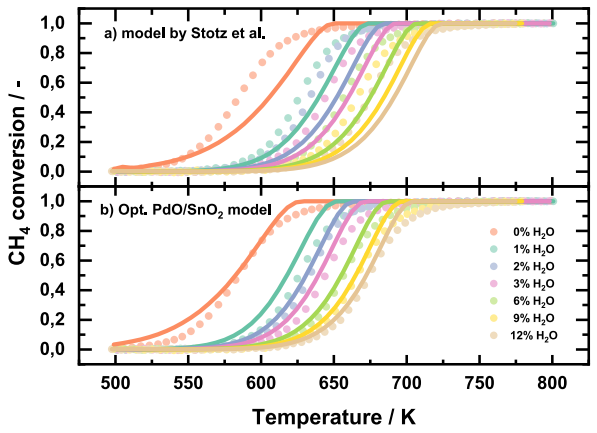

Figure 2. Experimental light-off data (dots) for a PdO/SnO_2 catalyst in 3200 ppm of CH_4, 10 vol % O_2, and balance N_2 with varying H_2O concentrations from 0 to 12 vol % at a linear temperature ramp of 3 K min^{-1} and a GHSV = 80,000 h^{-1} compared with simulation data (lines) obtained with (a) the model by Stotz et al.[42] and (b) the adjusted new model for PdO/SnO_2. Experimental data points reproduced from ref 19. Available under a CC-BY license. Copyright 2023, K. Keller, P. Lott, S. Tischer, M. Casapu, J.-D. Grunwaldt, and O. Deutschmann.

When comparing different catalyst formulations, existing models often diverge from experimental activity data, e.g., as can be seen in Figure 2a. Herein, an experimental light-off measurement of a PdO/SnO_2 powder catalyst sample is compared with the model proposed by Stotz et al.,[42] which is originally validated for an Al_2O_3-supported catalyst. Compared with the simulations (solid lines), the experimental data (denoted as points) clearly show higher conversions in the absence of water. Similarly, the model underpredicts the catalytic oxidation of methane in the presence of water and suggests conversions that are too low for all water concentrations subject to this study. Consequently, the water inhibition effect is overestimated. This deviation is expected as the original model developed for an Al_2O_3-supported catalyst did not consider any effect of the support and therefore cannot be used directly to simulate the catalytic performance of PdO/SnO_2.

Since catalyst formulation-related structural parameters, i.e., different accessible surface areas and particle sizes, were considered when applying the original model for PdO/SnO_2, the divergence of modeled and experimental data calls for an improvement of the model (Figure 2a). The microkinetic mechanism published by Stotz et al.[42] is based on first-principles, which does not include the influence of the support material. While the model matches the water inhibition observed for Al_2O_3-supported catalysts fairly well,[9,42] it neglects all the potentially beneficial properties of SnO_2 that are summarized in the Introduction and thus underestimates the actual performance of PdO/SnO_2 observed herein (Figure 2a).[19,55] Since the influence of such support-related effects may indirectly lay within the uncertainty of the energy barriers originating from DFT calculations,[48,50] fine-tuning of the specific set of kinetic parameters for all 39 reversible reactions to the experimentally measured conversion rates of the catalyst is justified.

In Figure 2b, the experimental data are compared to the simulation results obtained with the optimized model for PdO/SnO_2. Here, the automated reaction mechanism optimization was applied to capture the light-off behavior for the dry case as well as the shift of the light-off curve toward higher temperatures in the presence of water. As described in the Methods section, a set of independent but sensitive reactions is chosen to be subsequently optimized by the algorithm. Possible changes are highly limited for several reasons. First and foremost, the boundaries for the independent reaction parameters are set to ±1% of their value at any given iteration of the hopping procedure; therefore, the changes of the new microkinetic model should stay within a small range. Second, larger adjustments are allowed to occur mostly for the kinetically less significant reactions. The selected data set for the optimization process for the SnO_2 support comprised only the three different temperatures T_{10}, T_{50}, and T_{90}, i.e., the temperatures at 10%, 50%, and 90% methane conversion, obtained from the light-off curves in dry feed with 1 vol % H_2O. This input provided sufficient information for the objective function to obtain the best matching set of parameters. When the performance of the optimization process was tested by running simulations with the optimized model at different water concentrations up to 12

https://doi.org/10.1021/acscatal.5c00516
ACS Catal. 2025, 15, 6937−6952

Table 1. Kinetic Parameters of the Two-Site Mean Field Reaction Mechanism for CH_4 Oxidation Over PdO/SnO_2 in the Form of the Modified Arrhenius Expression[a]

Nr.	Adsorption/Desorption Reaction	s^0 / 1	β_f / 1	$E_{a,f}$ / kJ mol^{-1}	A_r	β_r / 1	$E_{a,r}$ / kJ mol^{-1}
R1	$CH_4(g) + (a) + (b) \rightleftarrows CH_3(a) + H(b)$	4.59E-02	-0.001	34.229	1.03E+21 $\frac{cm^2}{mol\,s}$	0.002	96.49
R2	$CH_4(g) + OH(a) + (a) \rightleftarrows CH_3(a) + H_2O(a)$	1.52E-02	0.001	28.766	7.21E+19 $\frac{cm^2}{mol\,s}$	-0.004	94.71
R3	$CH_4(g) + O(a) + (a) \rightleftarrows CH_3(a) + OH(a)$	3.05E-02	0.007	26.28	2.66E+20 $\frac{cm^2}{mol\,s}$	-0.03	191.23
R4	$O_2(g) + (a) \rightleftarrows O_2(a)$	5.68E-02	0	0	6.65E+15 $\frac{1}{s}$	-0.031	63.29
R5	$O_2(g) + vac(b) \rightleftarrows O(b)$	5.69E-02	0	0	7.01E+15 $\frac{1}{s}$	-0.027	159.86
R6	$H_2O(g) + O(a) + (a) \rightleftarrows 2OH(a)$	1.39E-01	0	0	3.21E+21 $\frac{cm^2}{mol\,s}$	0.013	199.38
R7	$H_2O(g) + (a) \rightleftarrows H_2O(a)$	1.42E-01	0	0	6.31E+12 $\frac{1}{s}$	0.045	100.38
R8	$CO_2(g) + (a) \rightleftarrows CO_2(a)$	5.04E-02	0	0	3.98E+14 $\frac{1}{s}$	0.029	65.73
Nr.	Surface Reaction	A_f / $\left(\frac{cm^2}{mol\,s}\right)$	β_f / 1	$E_{a,f}$ / kJ mol^{-1}	A_r / $\left(\frac{cm^2}{mol\,s}\right)$	β_r / 1	$E_{a,r}$ / kJ mol^{-1}
R9	$CH_3(a) + (b) \rightleftarrows CH_3(b) + (a)$	1.50E+22	0.008	129.63↓	3.74E+22	0.245	173.10↓
R10	$CH_3(b) + O(a) \rightleftarrows CH_2(b) + OH(a)$	1.24E+22	0.012	34.24↑	1.69E+22	-0.012	308.90↑
R11	$CH_3(b) + OH(a) \rightleftarrows CH_2(b) + H_2O(a)$	1.42E+22	-0.004	34.84↑	1.05E+22	0.004	210.50↓
R12	$CH_3(a) + O(a) \rightleftarrows CH_2OH(a) + (a)$	3.55E+21	0.016	31.28↑	3.68E+22	0.237	320.45↓
R13	$CH_3(a) + OH(a) \rightleftarrows CH_2(a) + H_2O(a)$	2.04E+21	0.004	73.21↓	1.17E+22	-0.004	114.87↓
R14	$CH_2(a) + OH(a) \rightleftarrows CH_2OH(a) + (a)$	3.34E+21	-0.004	12.73↑	3.26E+21	0.257	161.22↓
R15	$CH_2OH(a) + (b) \rightleftarrows CH_2O(a) + H(b)$	1.95E+22	0.012	12.66↑	3.35E+20	-0.012	57.24↓
R16	$CH_2O(a) + OH(a) \rightleftarrows CHO(a) + H_2O(a)$	5.53E+21	0.012	51.46↓	2.08E+22	-0.012	194.50↑
R17	$CHO(a) + OH(a) \rightleftarrows CO(a) + H_2O(a)$	5.96E+22	0.008	65.57↓	9.15E+21	-0.008	264.64↓
R18	$CH_3(a) + (b) \rightleftarrows CH_2(a) + H(b)$	1.81E+21	0	123.35↓	4.95E+22	0	161.34↓
R19	$CH_2(a) + (b) \rightleftarrows CH_2(b) + (a)$	1.25E+22	0	13.32↑	3.98E+21	0.253	190.78↓
R20	$CH_2(a) + (b) \rightleftarrows CH(a) + H(b)$	3.80E+22	0.008	115.49↑	2.90E+22	-0.008	167.94↑
R21	$CH(a) + (b) \rightleftarrows CHO(a) + vac(b)$	2.10E+21	0.008	24.54↓	1.832E+20	0.246	206.16↓
R22	$CH_2(b) + (a) \rightleftarrows CH_2O(a) + vac(b)$	2.12E+22	0.008	91.76↑	2.46E+20	-0.008	9.02↓
R23	$CH_2O(a) + (b) \rightleftarrows CHO(a) + H(b)$	3.33E+21	0.008	70.38↑	5.97E+22	-0.008	209.74↑
R24	$CHO(a) + (b) \rightleftarrows CO(a) + H(b)$	1.10E+23	0.004	55.33↓	8.02E+22	-0.004	250.71↓
R25	$CHO(a) + (b) \rightleftarrows CHO(b) + (a)$	2.73E+22	0.018	76.01↓	7.01E+21	-0.017	95.56↓
R26	$CHO(b) + (a) \rightleftarrows CO(b) + H(a)$	2.77E+21	-0.002	142.39↑	2.14E+21	0.002	267.83↑
R27	$CO(a) + (b) \rightleftarrows (a) + CO(b)$	1.32E+21	0.011	33.98↑	2.23E+21	-0.011	15.90↓
R28	$CO(b) + (a) \rightleftarrows CO_2(a) + vac(b)$	1.39E+21	0.01	42.74↑	9.54E+20	-0.01	79.20↑
R29	$H(b) + (a) \rightleftarrows OH(a) + vac(b)$	1.90E+22	0	126.37↓	4.20E+21	0	28.01↑
R30	$O_2(a) + (a) \rightleftarrows O(a) + O(a)$	3.87E+22	0.005	170.26↓	1.72E+21	-0.005	59.61↑
R31	$O(b) + (a) \rightleftarrows O(a) + (b)$	2.35E+22	0.027	116.88↑	1.75E+21	-0.027	110.70↑
R32	$O(a) + vac(b) \rightleftarrows (a) + (b)$	7.96E+21	0.02	48.27↓	1.40E+22	-0.02	249.32↓
R33	$O_2(a) + vac(b) \rightleftarrows O(a) + (b)$	1.21E+24	0.025	81.95↑	9.46E+22	-0.026	172.34↑
R34	$H(b) + (a) \rightleftarrows H(a) + (b)$	5.87E+22	0	150.02↑	9.39E+21	-0.002	117.70↓
R35	$CHO(b) + OH(a) \rightleftarrows H_2O(a) + CO(b)$	3.01E+22	0.001	2.12↓	3.06E+22	-0.001	163.57↑
R36	$CHO(b) + (a) \rightleftarrows HCOO(a) + vac(b)$	3.69E+21	0	11.74↑	1.19E+21	0	8.82↑
R37	$HCOO(a) + OH(a) \rightleftarrows CO_2(a) + H_2O(a)$	2.31E+23	0.011	185.32↑	4.99E+23	-0.011	386.14↑
R38	$HCOO(a) + (b) \rightleftarrows H(b) + CO_2(a)$	1.70E+23	0.007	177.58↓	1.74E+24	-0.008	374.72↑
R39	$H_2O(a) + (b) \rightleftarrows OH(a) + H(b)$	3.67E+21	0	13.65↑	1.74E+22	0.008	9.97↓

[a]The mechanism is fully thermodynamically consistent. Pd(cus) sites are denoted as (a), whereas O(cus) sites are represented by (b).[42]

https://doi.org/10.1021/acscatal.5c00516
ACS Catal. 2025, 15, 6937−6952

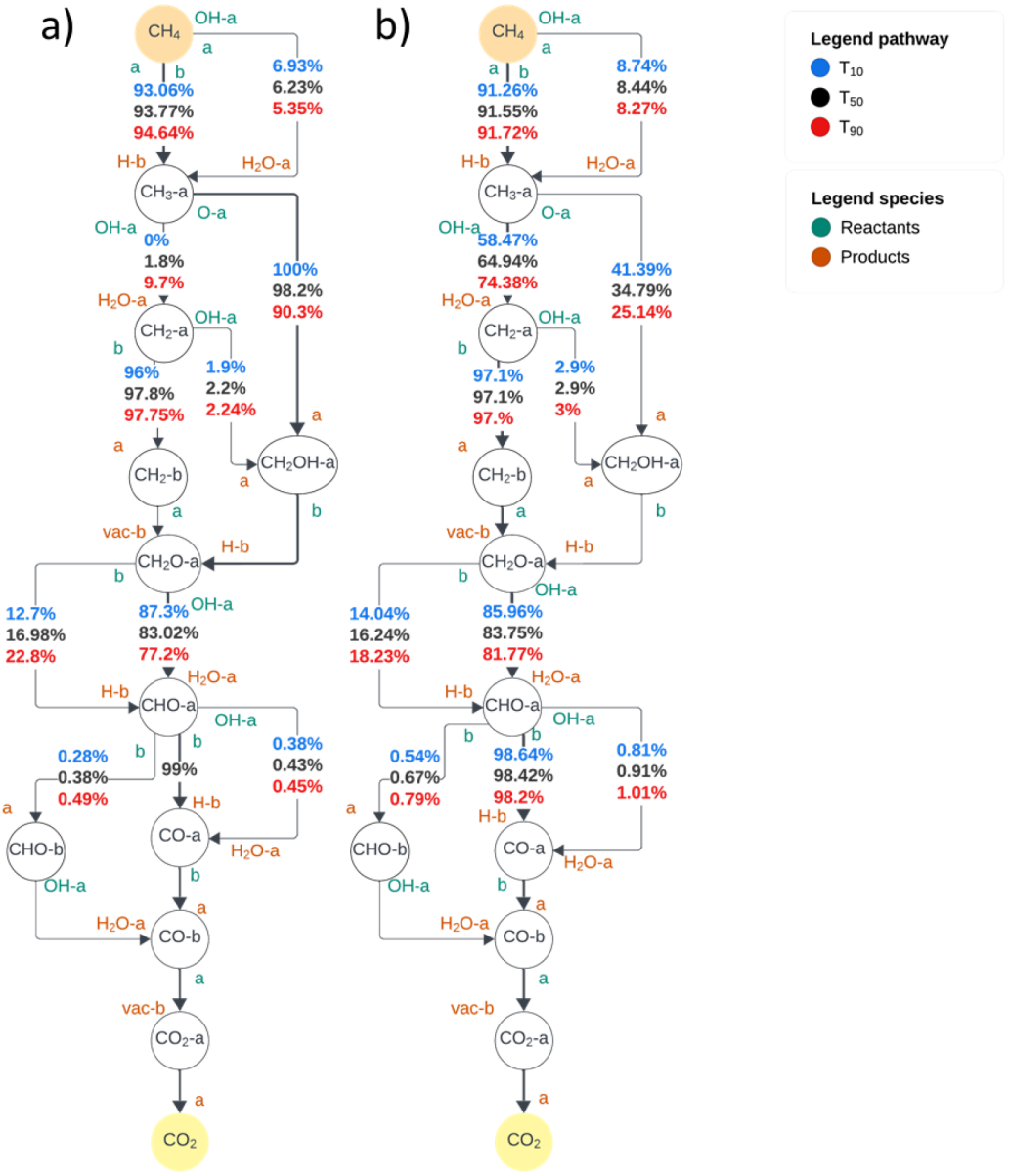

Figure 3. Simplified representation of the reaction flow analysis of the mechanism optimized for PdO/SnO_2 at different temperatures (T_{10}, T_{50}, T_{90}) and in the absence (a) and presence of 12 vol % H_2O (b) in 3200 ppm of CH_4, 10 vol % O_2, and balance N_2. A-sites denote a Pd_{cus}-site, b-sites denote an O_{cus}-site, whereas vac(b) represents an oxygen vacancy O^x_{cus} within the PdO surface as denoted in the original mechanism.[42]

vol %, a good fit was achieved for all studied H_2O concentrations and reactor temperatures (Figure 2b).

The resulting microkinetic mechanism for the SnO_2-adjusted model is listed in Table 1, with changes compared to the original mechanism in the activation barrier colored in red for absolute adjustments above 9%, in green below 4%, and in yellow for adjustments in between , with arrows indicating the direction of adjustment (increase ↑, decrease ↓), respectively. It is to be noted that the parameters in Table 1 correspond to the modified Arrhenius equation (eq S4). The associated surface rate expressions (in mol cm^{-2} s^{-1}) are given in eqs S5 and S8. The pre-exponential factors are expressed in units (cm^2 mol^{-1} s^{-1}) for all of the bimolecular reactions and (s^{-1}) for the unimolecular reactions (specifically $R4_r$, $R5_r$, $R7_r$, and $R8_r$). The sticking coefficients s^0 for the adsorption reactions and the temperature-dependent parameter β are dimensionless. The values are given for a reference temperature of 1 K and a surface site density of 3.553×10^{-9} mol cm^{-2}.

Among the reactions that had higher adjustments (shown in red), the highest absolute change was made in the activation barrier for reaction $R14_r$ (index r: reverse reaction): It led to a reduction in the activation energy value by 19 kJ mol^{-1}, corresponding to 0.20 eV and representing a reasonable change in comparison to the overall discussed uncertainty of the energy barriers originating from DFT calculations, e.g., caused by the electron correlation and exchange in the code,[62] which then potentially sums up to an uncertainty of around 20−30 kJ mol^{-1}.,[44,45] A more detailed analysis of the differences in activation energies for the optimized model can be found in Figure S6. In this work, the step size for the parameter search was kept relatively small in order to minimize deviation from the original parameters. Additionally, multiple local minima from the parameter search were analyzed to

https://doi.org/10.1021/acscatal.5c00516
ACS Catal. 2025, 15, 6937−6952

Table 2. Consumption Preference of O-a under Dry and Humid Conditions (12 vol % H_2O)

		Preference under dry conditions			Preference under humid conditions		
Nr.	Reaction	T_{10}, 543 K	T_{50}, 584 K	T_{90}, 621 K	T_{10}, 638 K	T_{50}, 674 K	T_{90}, 706 K
R6	a + O-a + H_2O = OH-a + OH-a	33.72%	36.14%	37.39%	78.1%	79.64%	81.96%
R12	CH_3-a + O-a = a + CH_2OH-a	46.25%	47.20%	44.21%	20.7%	17.37%	12.55%
R30	O-a + O-a = a + O_2-a	15.58%	8.55%	5.1%	0.2%	0.27%	0.3%
R32	vac-b + O-a = a + b	4.44%	8.10%	13.29%	1.03%	2.72%	5.18%

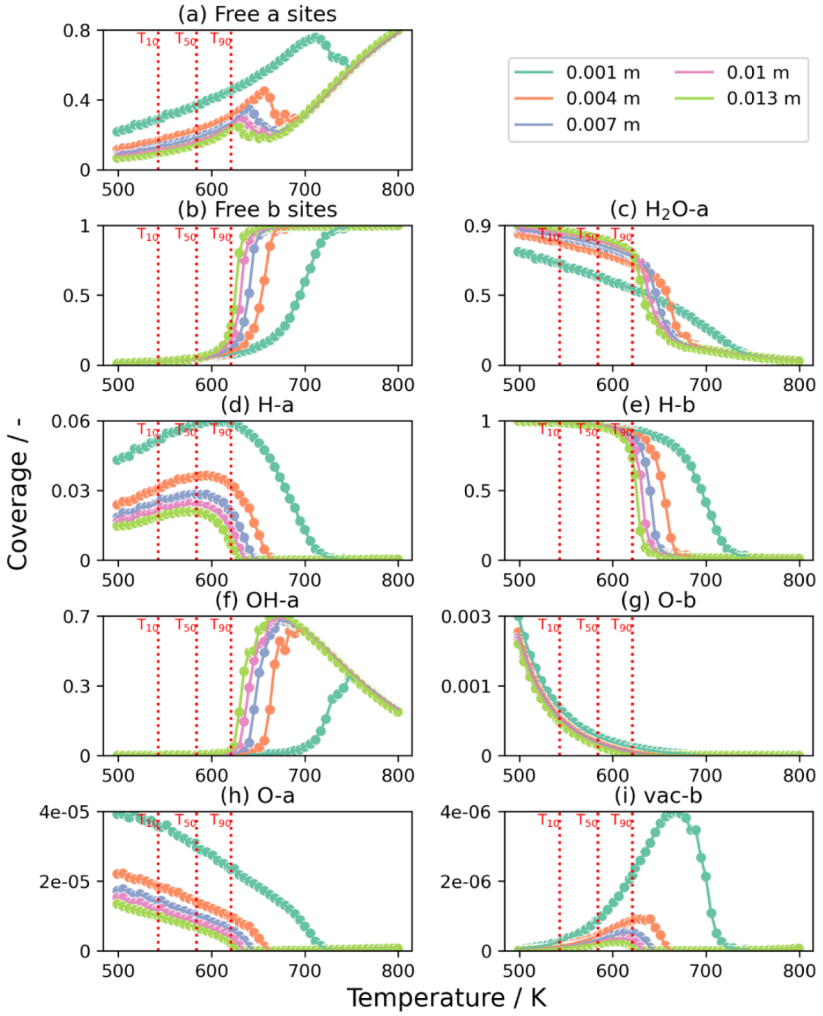

Figure 4. Simulated surface coverages under dry conditions (3200 ppm of CH_4, 10 vol % O_2, balance N_2; GHSV = 80 000 h^{-1}) of the most abundant species on a- and b-sites for different temperatures at different axial positions within the PdO/SnO_2 catalyst (packed bed): (a) Free a sites, (b) Free b sites, (c) H_2O-a species, (d) H-a species, (e) H-b species, (f) OH-a species, (g) O-b species, (h) O-a species, and (i) vac-b species.

identify the physically most realistic solution. However, to further enhance the discovery of physically realistic models by exploiting prior knowledge, methods such as the Bayesian Parameter Estimation, which accounts for both parameter and experimental data uncertainties,[63] or regularization techniques[64] to search for sparse solutions, i.e., minimum changes to the original parameters, may be beneficial.

In order to fully elaborate on the catalytic activity in the absence and presence of water, a reaction path analysis that identifies the dominant pathways on the surface for three different temperatures T_{10}, T_{50}, and T_{90} was conducted and is presented in Figure 3. Here, the evolution of crucial surface species toward CO_2(g) formation as well as the influence of water and higher temperatures on the preferred reaction pathway is shown. The preferred reaction paths under changing reaction conditions match the findings by Stotz et al.,[42] who concluded that methane oxidation occurs predominantly via two different reaction pathways that either involve hydroxyl-methyl intermediates (CH_2OH-a) or methylene intermediates (CH_2−a); in the mechanism, -a and -b represent two different surface sites as indicated in the microkinetic mechanism in Table 1. While the CH_2OH-a-assisted route (CH_4(g) → CH_3-a → CH_2OH-a → CH_2O-a → CHO-a → CO-a → CO-b → CO_2(g)) is responsible for methane oxidation at lower temperatures and under dry conditions, the CH_2-a-assisted route (CH_4(g) → CH_3-a → CH_2-a → CH_2-b → CH_2O-a → CHO-a → CO-a → CO-b → CO_2(g)) is mostly dominant at humid conditions and higher temperatures.[42] In general, it is not possible to deconvolute the effect of every change made during the automated optimization

https://doi.org/10.1021/acscatal.5c00516
ACS Catal. 2025, 15, 6937−6952

process because it is the combined effect of the changes in all the mechanism parameters that leads to a better prediction of the experimental data. One of the reactions that was subject to the biggest changes was reaction $R14_r$: the activation energy of the reaction was lowered, which suggests a pronounced shift of surface species from CH_2OH-a toward CH_2-a; this shift might lead to the enhancement of the wet pathway allowing to better describe the catalytic performance in the presence of water. Moreover, reaction $R25_r$ is adjusted to increase the rate of CHO-a species formation, which is the last step before CO formation on the surface, and ultimately leads toward CO_2(g). It should be pointed out that the sensitivity of each reaction must be considered. It is therefore observed that even with some larger changes to the initial parameters, the major reaction pathways remain unchanged.

As shown in Figure 3, in both dry and humid conditions, CH_4 most preferably adsorbs dissociatively over free a- and b-sites, which proceeds through reaction $R1_f$ (index f: forward reaction). The activation of CH_4 through OH-a ($R2_f$) is preferred only by less than 9% at all different temperatures, although its contribution under humid conditions is slightly higher compared to the dry case, most likely due to a higher availability of OH-a species. Subsequently, the two major pathways that are responsible for methane oxidation are shown quantitively for T_{10}, T_{50}, and T_{90} (Figure 3). While under dry conditions at 543 K, i.e., T_{10}, all adsorbed CH_3-species are further reacting toward CH_2OH-a through $R12_f$, only 90.3% of CH_3-a participate in this reaction at 621 K. Simultaneously, the contribution of the high-temperature pathway, i.e., $R13_f$ and CH_2-a species, increases to 9.7%, which agrees with the initial mechanism.[42] However, the CH_2OH-a-assisted pathway is less preferred compared to the CH_2-a-assisted pathway for all temperatures under humid conditions. At 638 K, corresponding to T_{10} in humid conditions, already 58.5% of CH_3-a species react to CH_2-a via $R13_f$, in comparison to 41.4% toward CH_2OH-a through $R12_f$. With increasing temperature even more CH_3-a surface species are consumed toward CH_2−a formation, which highlights the importance of the CH_2-a-assisted high-temperature reaction pathway especially in the presence of water.

In the dry pathway, the CH_3-a species interacts with O-a species to form CH_2OH-a; under humid conditions, however, the O-a species is preferentially consumed for water activation through oxidative dissociative adsorption from the gas phase, i.e., $R6_f$ leading to the formation of OH-a species. The results of the reaction flow analysis in terms of the consumption of O-a species within the reaction network are summarized in Table 2. The consumption share of O-a in $R6_f$ further increases with higher temperatures for both dry and humid conditions. This points to a change in the dominant reaction pathways that is due to the consumption preference of aqueous O-a for water activation rather than the formation of CH_2OH-a through R_{12f}.

Furthermore, Figures 4 and 5 show the most abundant surface intermediates under dry and humid conditions, respectively. The reduction of surface coverages and the absence of gradients in the reactor for the O-a species from dry to humid conditions further demonstrate that the O-a species are consumed for reactions other than $R12_f$. The low coverages of OH-a species under both conditions show that once formed it reacts quickly via $R2_f$, $R13_f$, and $R16_f$ toward CH_3-a, CH_2-a, and CHO-a formation, respectively, and consequently produces H_2O-a species on the surface of the catalyst.

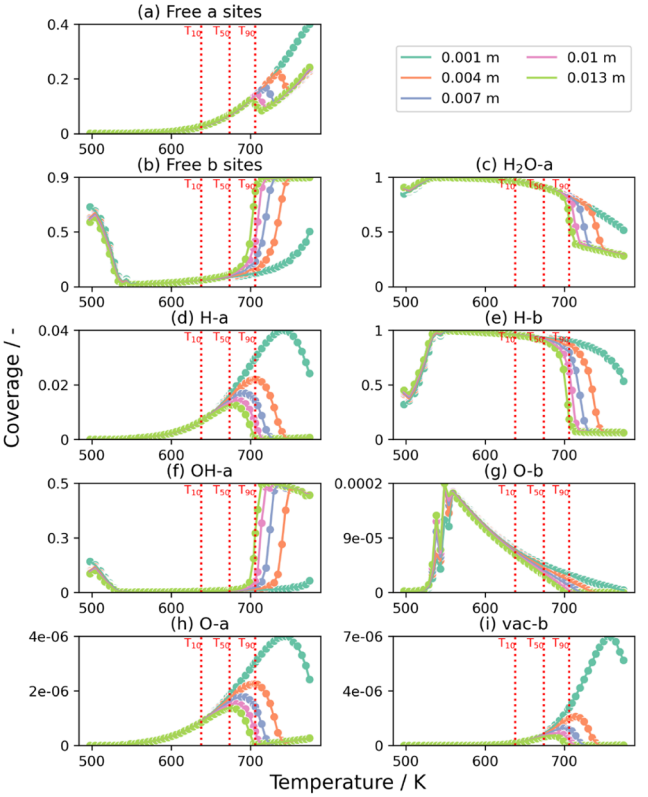

Figure 5. Simulated surface coverages under humid conditions (3200 ppm of CH_4, 10 vol % O_2, 12 vol % H_2O, balance N_2; GHSV = 80 000 h^{-1}) of the most abundant species on a- and b-sites for different temperatures at different axial position within the PdO/SnO_2 catalyst (packed bed): (a) Free a sites, (b) Free b sites, (c) H_2O-a species, (d) H-a species, (e) H-b species, (f) OH-a species, (g) O-b species, (h) O-a species, and (i) vac-b species.

The data shown in Figure 5 uncover that even in a dry feed that does not contain any water in the gaseous atmosphere, a-sites are mostly covered by water (H_2O-a; Figure 4c) and a small fraction of H-a species (Figure 4d) once the temperature is sufficiently high for methane conversion. Both surface species originate solely from the surface reaction itself. With H_2O coverages of over 80% at T_{50} and below, most a-sites are blocked by H_2O already at rather low temperatures (cf. Figure 4c). Although increasing temperatures facilitate the desorption of water and thus more a-sites become accessible, OH-a remains the predominant species on a-sites with a maximum coverage of 68% mainly via $R39_f$, $R29_f$, and $R6_f$ at temperatures around 650−700 K. Only once the temperature exceeds 700 K, ensuring complete oxidation of methane, a-sites become available again, as the chemical reactions and desorption processes are rather fast and mostly occur in the front zone near the catalyst inlet. The spatial profile of vac-b sites supports this conclusion as it shows the highest presence at the beginning of the reactor with increasing temperature (Figure 4i). The production of vac-b sites via $R28_f$ as a byproduct is the penultimate step for the production of CO_2 as CO_2-a species and hence also signifies methane conversion to CO_2. As depicted in Figure 4i, free b-sites become available once the overall conversion of methane is high at elevated temperatures. At low temperatures, the b-sites are almost entirely covered by the H-b species (Figure 4e) that form predominantly via $R39_f$ and from the hydrogen abstraction reactions during the oxidation process of methane. In turn, H-b species are

https://doi.org/10.1021/acscatal.5c00516
ACS Catal. 2025, 15, 6937−6952

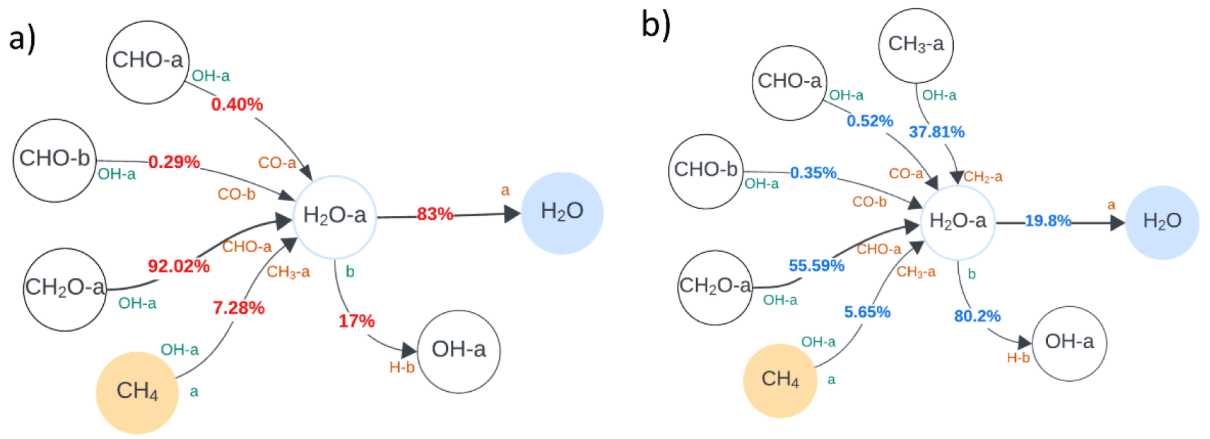

Figure 6. Reaction preference for consumption and production of H_2O-a species over PdO/SnO_2 at T_{10} for (a) dry conditions at 543 K (red) and (b) humid conditions at 638 K (blue); reaction gas mixture: 3200 ppm of CH_4, 10 vol % O_2, 0/12 vol % H_2O, and balance N_2.

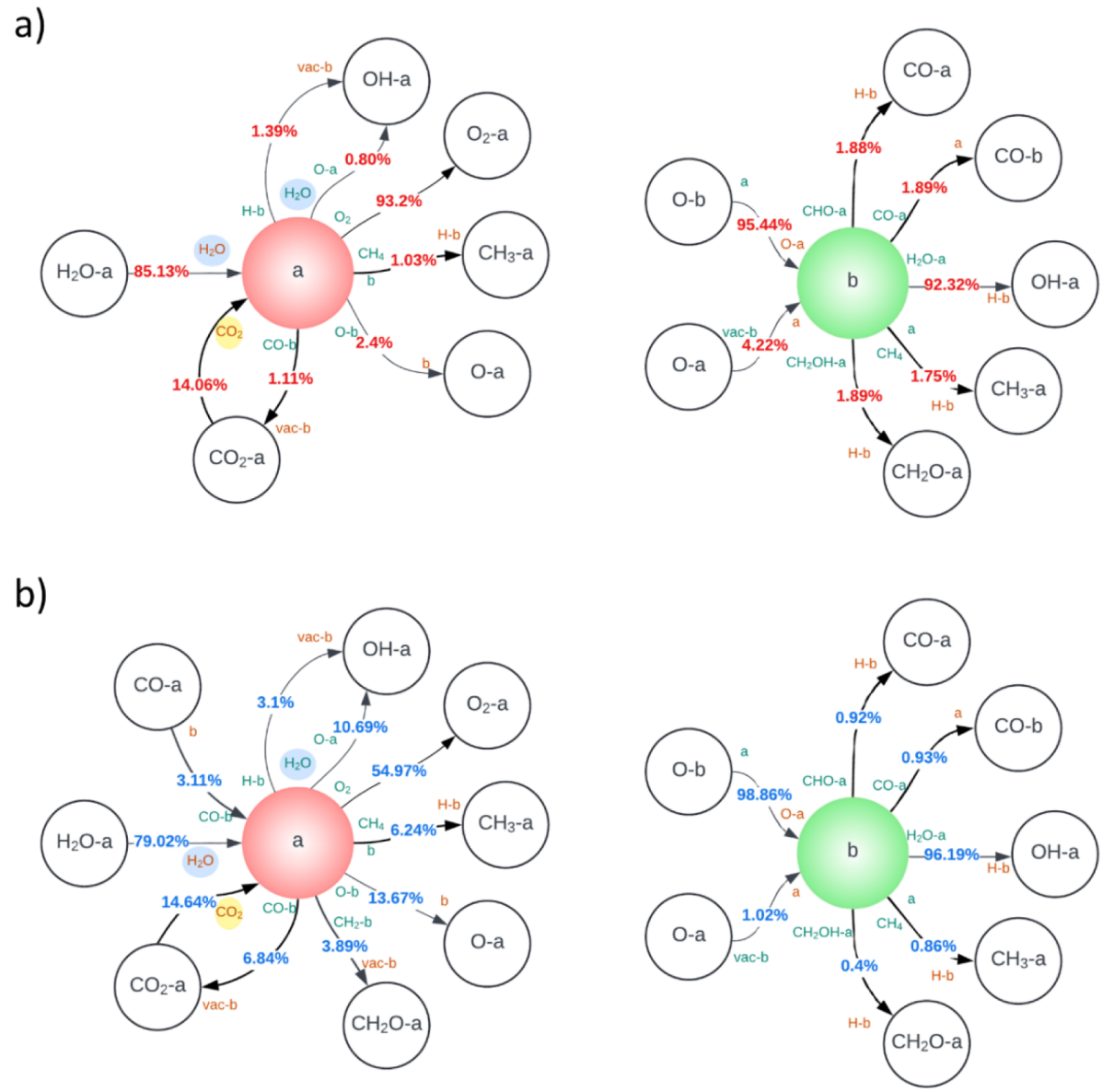

Figure 7. Reaction preferences for a- and b-sites over PdO/SnO_2 at T_{10} for (a) dry conditions at 543 K (top, red) and (b) humid conditions at 638 K (bottom, blue); reaction gas mixture: 3200 ppm of CH_4, 10 vol % O_2, 0/12 vol % H_2O, and balance N_2.

https://doi.org/10.1021/acscatal.5c00516
ACS Catal. 2025, 15, 6937−6952

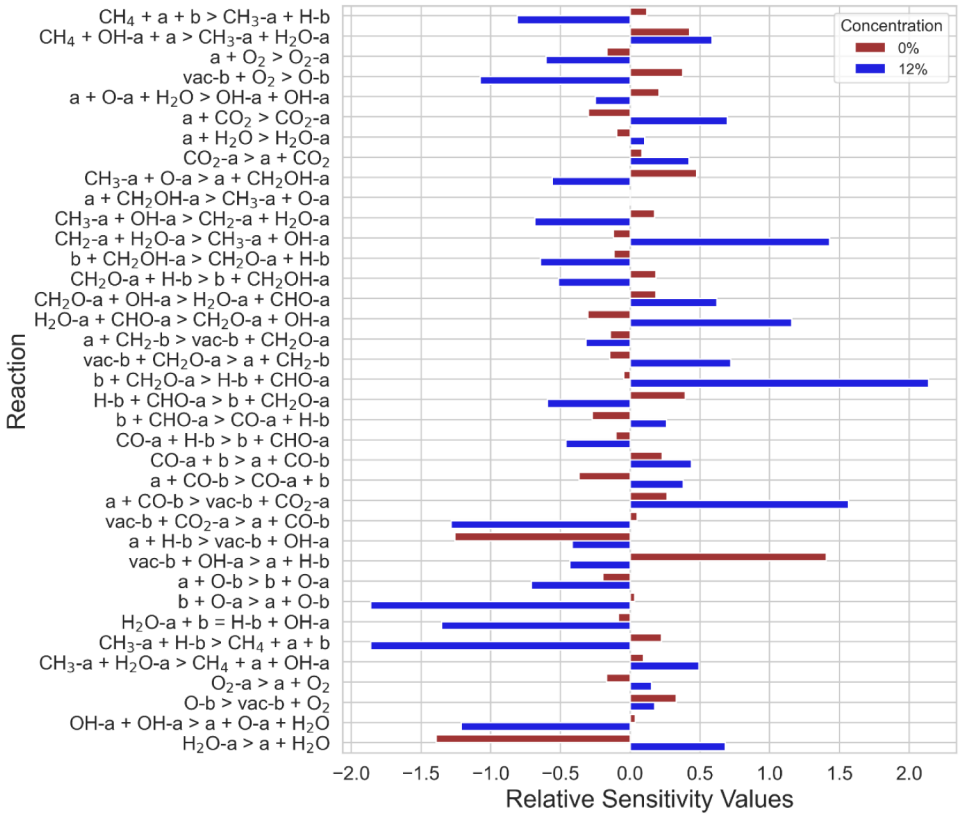

Figure 8. Sensitivity analysis at T_{10} for the methane oxidation mechanism over PdO/SnO_2 in the absence of water (red) and presence of 12 vol % water (blue) in 3200 ppm of CH_4, 10 vol % O_2, and balance N_2.

consumed mostly via $R29_f$ by interaction with free a-sites to produce vac-b and OH-a species, which becomes increasingly relevant at an elevated temperature. O-b species are formed via vacancy regeneration according to $R5_f$ and are subsequently consumed to generate free b-sites ($R31_f$). Thus, with increasing temperature, H-b coverages decrease, and free b-sites are available.

In humid reaction conditions, i.e., in the presence of 12 vol % of water, over 98% of active a-sites are expected to be blocked by H_2O (Figure 5c) originating from the oxidation reaction on the one hand, but mostly due to H_2O adsorption from the gas phase. Herein, OH-a species remain low in coverage, which only ramps up at higher temperatures above 700 K (Figure 5f). However, H_2O-a species remain the most abundant species until the temperature exceeds 700 K, which is almost T_{90} and thus demonstrates the pronounced inhibition effect of water on the surface of the catalyst. Only at even higher temperatures does the occupation of a-sites decrease due to desorption of surface adsorbates, herewith showing the same trend observed for dry conditions. Similar to the dry case, H-b species are the most abundant species on b-sites at lower temperatures (Figure 5e). However, since most a-sites are blocked by adsorbed H_2O (Figure 5c) and no coverages of vac-b are predicted by the model (Figure 5i), the observed early accumulation of H-b does not signify CH_4 activation and subsequent adsorption, but rather the influence of H_2O on the surface of the catalyst. Nonetheless, at temperatures above 650 K and conversion rates over 50% mostly free a-sites are accessible (Figure 5a) because the overall reaction and the desorption processes of reaction products and water are comparably fast.

In this regard, it is important to understand where surface H_2O on a-sites originates from, which is described using the effective integral rates of the consumption and production reactions for H_2O-a as illustrated in Figure 6 for the dry and wet cases at their respective T_{10}. As depicted in Figure 6a for the dry case at 543 K, 7.28% of H_2O-a species are produced through the adsorption of CH_4 over OH-a and a-sites according to reaction $R2_f$. However, the majority of H_2O-a species are produced from CH_2O-a species further reacting to CHO-a (92.02%; $R16_f$). As already discussed above, mainly two reaction routes are responsible for methane oxidation on the surface of the catalyst, namely, $R12_f$ (CH_2OH-a assisted) and $R13_f$ (CH_2-a assisted). These pathways are combined again with reaction $R16_f$ to form CHO-a. Due to the low activity at T_{10} and the absence of water in dry conditions, mostly the CH_2OH-a-assisted route is preferred and accounts for methane oxidation at lower temperatures. The relevance of these reaction pathways changes under humid conditions and thus a higher T_{10} temperature of 638 K (Figure 6b). With more methane being oxidized over the CH_2-a-assisted pathway and a production of 38% of H_2O present on a-sites via $R13_f$, the contribution of $R16_f$ reduces compared to the dry case to only 56%.

Furthermore, the path preferences presented in Figure 7 clearly demonstrate that the b-sites follow the same pattern in both dry and humid conditions, with a slightly higher preference to $R39_f$ (92.32% in the dry case and 96.19% in the wet case), i.e., H-adsorption from a b-site toward OH-a and H-b, for consumption and regeneration through $R31_f$, i.e., oxygen exchange from O-b to a free a-site (95.44% in the dry case and 98.86% in the wet case). However, the regeneration

https://doi.org/10.1021/acscatal.5c00516
ACS Catal. 2025, 15, 6937−6952

of a-sites via H_2O desorption is lower for the wet case with 79.02% as compared to 85.13% for absence of water, which can be attributed to the humid conditions in the presence of 12 vol % H_2O in the gas phase. Since the availability of free a-sites is generally low, the rate of O_2 adsorption decreases significantly even though the temperature is higher in the wet case from 93.20% to 54.97%. As a result, the relevance of the oxidative dissociation adsorption of water via $R6_f$ increases to 10.69%.

Ultimately, a sensitivity analysis for the mechanism adjusted for PdO/SnO_2 and the effect of absence and presence of water is presented in Figure 8. For dry conditions, although no additional water is present in the gas phase and is exclusively produced during the oxidation reaction itself, water desorption on a-sites and the reactions $R29_f$ and $R29_r$ involving H-b species are most sensitive. Under consideration of the surface coverages, H-b was already shown to be a main indicator for CH_4 adsorption and activation on the surface of the catalyst. Therefore, in the absence of water they remain the most sensitive reactions for the adjusted new microkinetic model. For the wet case, as shown in Figure 8, different reactions that predominantly involve H_2O species and their derivatives on both a- and b-surface sites are considered sensitive. Especially at lower temperatures around T_{10} the surface is mostly covered and blocked with these surface species, highlighting why the catalytic activity during methane oxidation should always be discussed in the presence of water originating from the gas phase.

Methane Oxidation Over ZrO_2 Supported PdO Catalysts. In comparison to the SnO_2-supported sample, the overall performance of the ZrO_2-supported methane oxidation catalyst during the activity tests is slightly shifted toward higher temperatures (Figure 9). Here, T_{50} is approximately 590 K in dry reaction conditions and almost full conversion is achieved only above 650 K. The pronounced inhibition effect in the presence of 12 vol % H_2O shifts T_{50} toward 698 K, which is an increase by 24 K compared to the SnO_2-supported catalyst. Nonetheless, PdO/ZrO_2 catalysts can outperform conventional

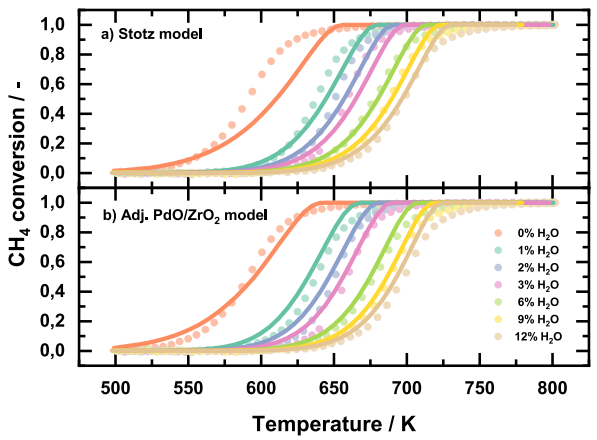

Figure 9. Experimental light-off data (dots) for a PdO/ZrO_2 catalyst in 3200 ppm of CH_4, 10 vol % O_2, and balance N_2 with varying H_2O concentrations from 0 to 12 vol % at a linear temperature ramp of 3 K min^{-1} and a GHSV = 80 000 h^{-1} compared with simulation data (lines) obtained with (a) the model by Stotz et al.[42] and (b) the adjusted new model for PdO/ZrO_2. Experimental data points reproduced from ref 19. Available under a CC-BY license. Copyright 2023, K. Keller, P. Lott, S. Tischer, M. Casapu, J.-D. Grunwaldt, and O. Deutschmann.

Al_2O_3 samples according to the literature,[19,26,65] as can be seen in the comparison with the model by Stotz et al.[42] in the upper part of Figure 9a. Due to the pronounced water inhibition that persists also at higher temperatures, the initial model that was originally developed for PdO/Al_2O_3 catalysts matches the experimental light-off data obtained for PdO/ZrO_2 in the presence of water rather well. However, the microkinetic mechanism fails to accurately describe the performance in dry conditions: methane conversion is underpredicted significantly, which calls for an optimization of the microkinetic model. With the help of an automated optimization tool, a new set of mechanism parameters is generated that is tailored to capture the catalytic activity of PdO/ZrO_2 methane oxidation catalysts over a broad range of conditions and that considers water inhibition. Since the accessible surface area of the catalyst is an input parameter of the model, therefore influencing the simulated conversion rates due to the underlying Mars–van Krevelen mechanism,[23,66] the catalytic activity in general can be further dependent on the diameter of the active noble metal particles[67] and morphology.[68] Therefore, increased catalytic activity is also observed for slightly bigger particles such as PdO on ZrO_2, as described in Table S1, correlating with the weakened Pd–O bond strength.[23,66]

Regarding the adjusted model for PdO/ZrO_2 that is depicted in Figure 9b, the optimization of the kinetic parameters improved the overall agreement with the experimental results in the absence of water, while the accuracy in humid reaction conditions remained fairly high. The underlying physicochemical phenomena are reflected in the adjusted mechanism, as shown in Table 3.

Surface species originating from CH_3-a are most decisive for the catalytic activity, as they mark the starting point for either the dry/low-temperature pathway (CH_2OH-a assisted) or the wet/high-temperature pathway (CH_2-a assisted). For an improved accuracy in the absence of water, however, a shift from the CH_2-a assisted to the CH_2OH-a-assisted pathway is required to improve catalytic conversion at lower temperatures, which is achieved through the increase in the energy barriers of reactions $R13_f$, $R14_r$, and $R18_f$. Notably, analyzing all shown changes within the new microkinetic model is not possible as discussed before because the overall optimization routine and methodology including the smaller adjustments are influential in contributing to the presented results. However, the biggest changes made in the activation energies are presented in Figure S7. Figure S8 also compares the energies for the reactions involved in the dominant reaction pathways for the parameters of both the supports. Ultimately, the changes in the microkinetic model affect the dominant reaction pathways, i.e., the two oxidation routes involving CH_2OH-a and CH_2-a intermediates, as discussed in the following.

Most kinetic parameters were algorithmically optimized to better predict the experimental values, especially under dry conditions. This effect of improved catalytic activity in the absence of water for the model adjusted for PdO/ZrO_2 is depicted in the reaction flow analysis shown in Figure 10. In contrast to the mechanism that was optimized for PdO/SnO_2 focusing on an accurate description especially at elevated temperatures under dry conditions, with the CH_2-a oxidation route being most significant, and 10% of CH_3-a species being converted to CH_2-a at T_{90}, for the ZrO_2 model, however, shows the CH_2OH-a-assisted route as the dominant pathway with a ratio of over 98% for all depicted temperatures. This demonstrates how the kinetic parameter adjustments primarily

https://doi.org/10.1021/acscatal.5c00516
ACS Catal. 2025, 15, 6937–6952

Table 3. Kinetic Parameters of the Two-Site Mean Field Reaction Mechanism for CH_4 Oxidation over PdO/ZrO_2 in the Form of the Modified Arrhenius Expression[a]

Nr.	Adsorption/Desorption Reaction	s^0 / 1	β_f / 1	$E_{a,f}$ / kJ mol^{-1}	A_r	β_r / 1	$E_{a,r}$ / kJ mol^{-1}
R1	$CH_4(g) + (a) + (b) \rightleftarrows CH_3(a) + H(b)$	0.049	-0.001	32.56	1.03E+21 $\frac{cm^2}{mol\,s}$	0.003	98.26
R2	$CH_4(g) + OH(a) + (a) \rightleftarrows CH_3(a) + H_2O(a)$	0.015	0.001	28.87	6.66E+19 $\frac{cm^2}{mol\,s}$	-0.003	96.79
R3	$CH_4(g) + O(a) + (a) \rightleftarrows CH_3(a) + OH(a)$	0.032	0.007	25.88	2.67E+20 $\frac{cm^2}{mol\,s}$	-0.029	192.12
R4	$O_2(g) + (a) \rightleftarrows O_2(a)$	0.059	0	0.00	3.91E+15 $\frac{1}{s}$	0.051	52.70
R5	$O_2(g) + vac(b) \rightleftarrows O(b)$	0.057	0	0.00	5.73E+15 $\frac{1}{s}$	0	156.69
R6	$H_2O(g) + O(a) + (a) \rightleftarrows 2OH(a)$	0.144	0	0.00	3.63E+21 $\frac{cm^2}{mol\,s}$	0.013	199.52
R7	$H_2O(g) + (a) \rightleftarrows H_2O(a)$	0.140	0	0.00	6.40E+12 $\frac{1}{s}$	0.045	101.21
R8	$CO_2(g) + (a) \rightleftarrows CO_2(a)$	0.049	0	0.00	5.93E+14 $\frac{1}{s}$	-0.025	72.16
Nr.	Surface Reaction	A_f / $\left(\frac{cm^2}{mol\,s}\right)$	β_f / 1	$E_{a,f}$ / kJ mol^{-1}	A_r / $\left(\frac{cm^2}{mol\,s}\right)$	β_r / 1	$E_{a,r}$ / kJ mol^{-1}
R9	$CH_3(a) + (b) \rightleftarrows CH_3(b) + (a)$	1.56E+22	0	129.65↓	2.43E+23	-0.008	183.32↑
R10	$CH_3(b) + O(a) \rightleftarrows CH_2(b) + OH(a)$	1.25E+22	0.012	33.91↑	1.83E+22	-0.006	306.61↑
R11	$CH_3(b) + OH(a) \rightleftarrows CH_2(b) + H_2O(a)$	1.44E+22	-0.007	35.24↑	1.08E+22	0.007	209.62↓
R12	$CH_3(a) + O(a) \rightleftarrows CH_2OH(a) + (a)$	3.55E+21	0.016	30.97↑	2.15E+23	0.002	347.59↑
R13	$CH_3(a) + OH(a) \rightleftarrows CH_2(a) + H_2O(a)$	2.15E+21	-0.005	80.52↑	1.10E+22	0.005	109.56↓
R14	$CH_2(a) + OH(a) \rightleftarrows CH_2OH(a) + (a)$	3.42E+21	-0.004	12.73↑	2.05E+22	0.004	201.99↑
R15	$CH_2OH(a) + (b) \rightleftarrows CH_2O(a) + H(b)$	1.94E+22	0.012	12.44↓	3.35E+20	-0.012	57.69↑
R16	$CH_2O(a) + OH(a) \rightleftarrows CHO(a) + H_2O(a)$	5.64E+21	0.012	51.51↓	2.16E+22	-0.012	197.16↑
R17	$CHO(a) + OH(a) \rightleftarrows CO(a) + H_2O(a)$	6.12E+22	0.008	66.50↑	8.32E+21	0.01	270.80↑
R18	$CH_3(a) + (b) \rightleftarrows CH_2(a) + H(b)$	2.08E+21	-0.019	139.38↑	5.20E+22	0	166.19↑
R19	$CH_2(a) + (b) \rightleftarrows CH_2(b) + (a)$	1.25E+22	0	13.26↑	2.85E+22	-0.004	212.27↑
R20	$CH_2(a) + (b) \rightleftarrows CH(a) + H(b)$	3.80E+22	0.008	111.22↓	2.97E+22	-0.008	165.47↑
R21	$CH(a) + (b) \rightleftarrows CHO(a) + vac(b)$	2.08E+21	0.008	24.81↓	1.23E+21	-0.008	246.47↑
R22	$CH_2(b) + (a) \rightleftarrows CH_2O(a) + vac(b)$	2.21E+22	0.004	75.48↓	2.41E+20	-0.008	8.94↓
R23	$CH_2O(a) + (b) \rightleftarrows CHO(a) + H(b)$	3.24E+21	0.008	67.11↓	6.03E+22	-0.008	210.53↑
R24	$CHO(a) + (b) \rightleftarrows CO(a) + H(b)$	1.20E+23	-0.014	55.92↑	7.95E+22	-0.004	257.99↑
R25	$CHO(a) + (b) \rightleftarrows CHO(b) + (a)$	3.33E+22	0	86.57↑	6.86E+21	-0.018	108.38↑
R26	$CHO(b) + (a) \rightleftarrows CO(b) + H(a)$	2.76E+21	-0.002	140.68↓	2.17E+21	0.001	269.15↑
R27	$CO(a) + (b) \rightleftarrows (a) + CO(b)$	1.36E+21	0.011	33.13↓	2.20E+21	-0.011	16.23↓
R28	$CO(b) + (a) \rightleftarrows CO_2(a) + vac(b)$	1.38E+21	0.01	42.48↑	9.45E+20	-0.01	76.88↓
R29	$H(b) + (a) \rightleftarrows OH(a) + vac(b)$	1.78E+22	0	129.63↓	4.24E+21	0	27.59↓
R30	$O_2(a) + (a) \rightleftarrows O(a) + O(a)$	3.97E+22	0.006	172.32↓	1.79E+21	-0.005	58.41↓
R31	$O(b) + (a) \rightleftarrows O(a) + (b)$	2.92E+22	0	119.91↑	1.47E+21	0	104.59↓
R32	$O(a) + vac(b) \rightleftarrows (a) + (b)$	7.97E+21	0.02	46.14↓	1.35E+22	-0.02	248.72↓
R33	$O_2(a) + vac(b) \rightleftarrows O(a) + (b)$	1.22E+24	0.026	79.53↓	9.27E+22	-0.025	168.21↓
R34	$H(b) + (a) \rightleftarrows H(a) + (b)$	6.13E+22	0.002	146.69↓	9.29E+21	-0.001	111.79↓
R35	$CHO(b) + OH(a) \rightleftarrows H_2O(a) + CO(b)$	2.97E+22	0.001	2.16↓	3.17E+22	-0.001	167.74↑
R36	$CHO(b) + (a) \rightleftarrows HCOO(a) + vac(b)$	3.59E+21	0	11.74↑	1.23E+21	0	8.47↓
R37	$HCOO(a) + OH(a) \rightleftarrows CO_2(a) + H_2O(a)$	2.34E+23	0.011	182.15↓	4.98E+23	-0.011	385.41↑
R38	$HCOO(a) + (b) \rightleftarrows H(b) + CO_2(a)$	1.67E+23	0.007	179.87↑	1.73E+24	-0.007	380.91↑
R39	$H_2O(a) + (b) \rightleftarrows OH(a) + H(b)$	3.62E+21	0	12.49↓	1.76E+22	0.008	10.27↑

[a]The mechanism is fully thermodynamically consistent. Pd(cus) sites are denoted as (a), whereas O(cus) sites are represented by (b).[42]

https://doi.org/10.1021/acscatal.5c00516
ACS Catal. 2025, 15, 6937−6952

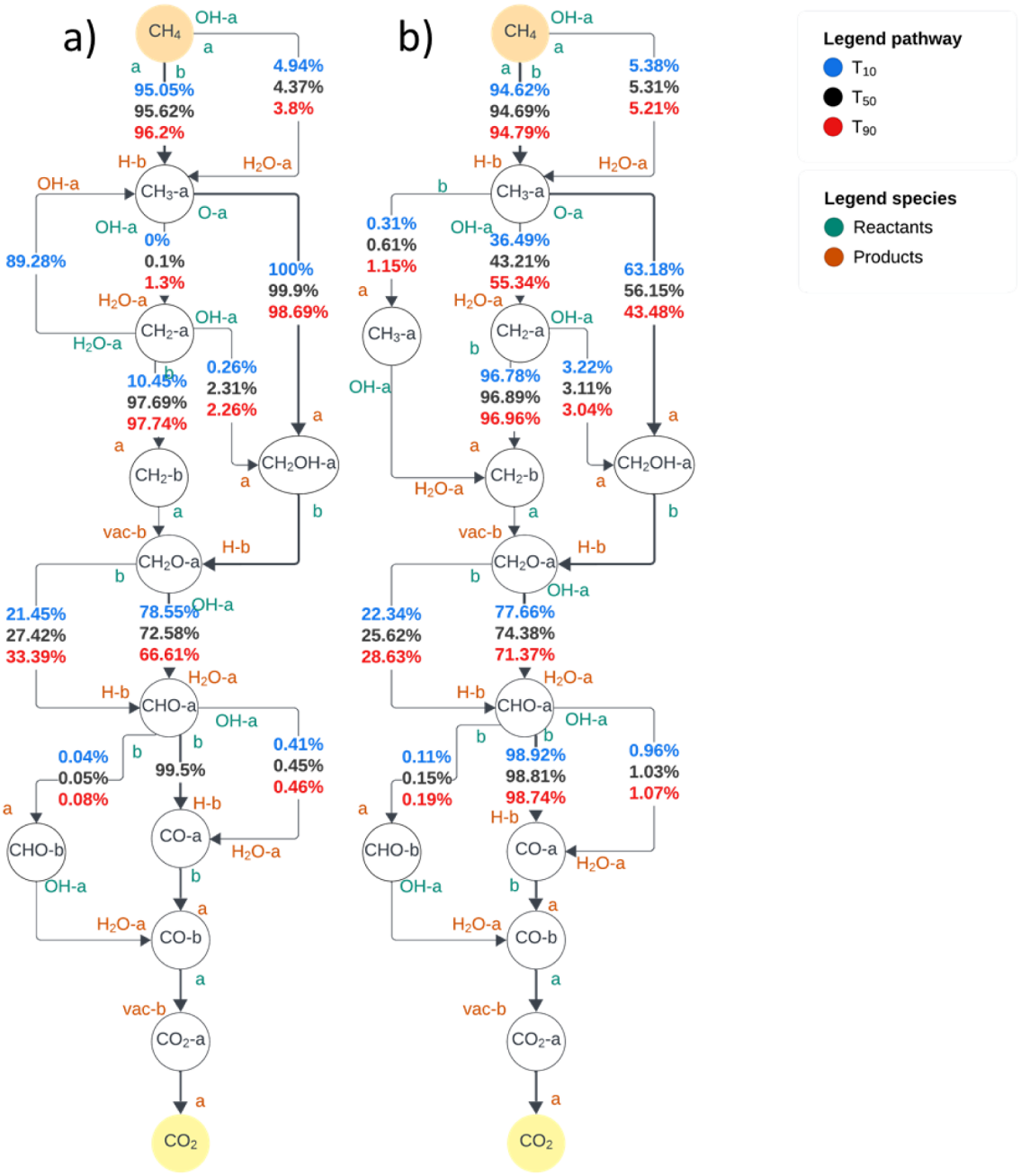

Figure 10. Simplified representation of the reaction flow analysis of the mechanism optimized for PdO/ZrO_2 at different temperatures (T_{10}, T_{50}, T_{90}) and in the absence (a) and presence of 12 vol % H_2O (b) in 3200 ppm of CH_4, 10 vol % O_2 and balance N_2. A-sites denote a Pd_{cus}-site, b-sites denote an O_{cus}-site, whereas vac(b) represents an oxygen vacancy O^{x}_{cus} within the PdO surface as denoted in the original mechanism.[42]

affect the CH_2OH-a-assisted pathway, thereby improving the methane conversion under dry conditions. Simultaneously, although the model's accuracy in the presence of water is unaffected, the reaction flow analysis under these conditions shows that over PdO/ZrO_2 the CH_2OH-a-assisted pathway is still the dominant pathway, albeit the CH_2-a-assisted pathway significantly contributes to the catalytic activity under dry conditions. As the temperature increases from T_{10} to T_{90}, the CH_2-a route becomes more prominent and eventually surpasses the CH_2OH-a route, making it the preferred reaction path at T_{90}. Therefore, the algorithmic optimization of the mechanism toward a more accurate description in dry conditions, while maintaining the inhibition effect in the presence of water, leads to different ratios between the two reaction pathways on the one hand and to slight changes in the species coverages in comparison to the PdO/SnO_2 mechanism.

Due to the change in the mechanism parameters, different coverages for the dry and wet cases are calculated from the simulations for the PdO/ZrO_2-adjusted model and shown in Figures S2 and S3. The coverages for the most abundant surface intermediates are qualitatively similar in their spatial profiles compared to the SnO_2 model (cf. Figures 4, 5). Furthermore, the surface coverages of free b-sites and OH-a species, which are essential for the production of CH_2-a species through $R13_f$ and $R18_f$, are similarly developed (cf. Figures 4, 5, S2, and S3) for both models. Similar trends are also observed for the production and consumption of H_2O-a sites as shown in Figure S4 (cf. Figure 6). Here, at dry conditions

https://doi.org/10.1021/acscatal.5c00516
ACS Catal. 2025, 15, 6937−6952

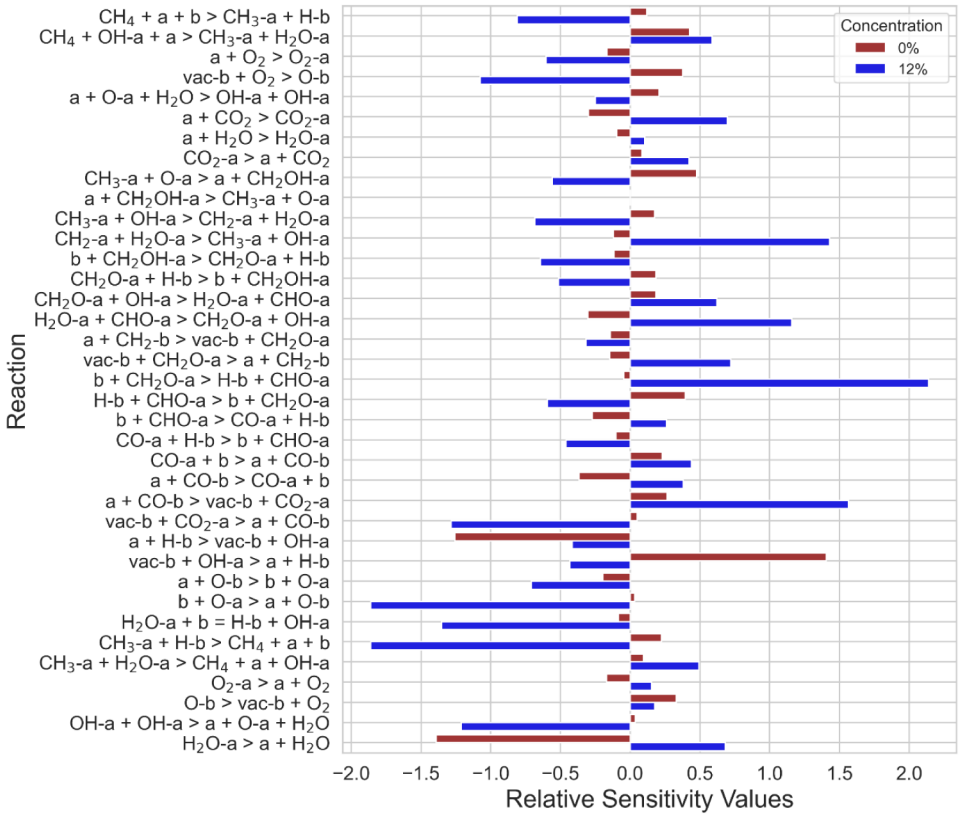

Figure 11. Sensitivity analysis at T_{10} for the methane oxidation mechanism over PdO/ZrO_2 in the absence of water (red) and presence of 12 vol % water (blue) in 3200 ppm of CH_4, 10 vol % O_2, and balance N_2.

similar ratios compared to the PdO/SnO_2-adjusted model are observed; however, for the PdO/ZrO_2 catalyst, a higher production of OH-a compared to simple H_2O desorption is found for the consumption of H_2O-a sites. In humid conditions, more H_2O-a is produced from CH_2O-a ($R16_f$) and less from CH_3-a ($R13_f$), however, also the water desorption is increased for this case. For the reaction preferences of a- and b-sites shown in Figure S5, the consumption and production of both sites are similar to the ones described for the PdO/SnO_2-model (cf. Figure 7); the only difference is found in the production of slightly more OH-a species through $R39_f$ and the adsorption of hydrogen on a free b-site in dry conditions.

A comparison of the sensitivity analysis of the new microkinetic mechanisms, i.e., for PdO/SnO_2 (Figure 8) and PdO/ZrO_2 (Figure 11), uncovers differences regarding the most sensitive reactions. For PdO/ZrO_2, the a- and b-site-assisted CH_4 activation toward CH_3-a plays a major role in the mechanism under both the dry and humid conditions. Additionally, $R13_r$ and the further reaction of CHO-a toward CO-a, which mark the last steps toward CO_2 formation, show their sensitive character. Under humid conditions, however, the sensitivity analysis again shows more evenly distributed values particularly focusing on O-a sites through $R31_r$ and water desorption reactions.

CONCLUSIONS

The study investigated how different support materials affected the catalytic activity during methane oxidation by comparing them to traditional Al_2O_3-based PdO catalysts. Using microkinetic modeling, it highlights the complex interplay of parameters in the Arrhenius expression and the impact on simulation results. The study shows that using SnO_2 or ZrO_2 as a support material can improve catalytic activity and methane conversion, even in the presence of water. Despite potential inhibition from hydroxyl formation on the support, the results demonstrate that reactions on the PdO surface are significantly influenced by the different support materials. Therefore, a previously published microkinetic model originally developed for describing the total oxidation of methane over Al_2O_3-supported PdO-based systems[42] was modified to capture the performance of PdO/SnO_2 and PdO/ZrO_2 catalysts, including the inhibiting effect of water vapor. Here, two independent sets of microkinetic data for a detailed reaction mechanism are presented, numerically studied with packed-bed reactor models, and compared to experimentally determined activity data obtained in the absence and presence of various water concentrations. An automated reaction mechanism optimization approach was used to fine-tune the original mechanism with the best set of the total 78 reactions and 234 parameters for the dual-site microkinetic mechanism. The new thermodynamically consistent models for PdO/SnO_2 and PdO/ZrO_2 allow to describe light-off measurements with good accuracy. The analysis of the surface coverages revealed the importance of H_2O-a species, which seem to block the a-sites (denoting unsaturated Pd sites in PdO particles) to a higher extent under humid reaction conditions. Two different reaction routes and particularly important surface species were identified by a reaction flow analysis, i.e., CH_2OH-a, which is relevant at lower temperatures, and CH_2-a, which is mostly present at higher temperatures and in humid conditions. However, it was found that the change in the two dominant reaction pathways is

https://doi.org/10.1021/acscatal.5c00516
ACS Catal. 2025, 15, 6937−6952

mostly caused by the preference of O-a sites for water activation, even for the dry case with no additionally dosed water, therefore referring to H_2O as the product of the oxidation reaction itself. Ultimately, the sensitivity analysis conducted for both mechanisms illustrates the impact of temperature, i.e., T_{10} differs for dry and humid conditions, and the change of the kinetic parameters toward sensitive reactions of the two newly generated mechanisms.

The derived microkinetic reaction kinetics for two PdO-based catalysts serve as a further example for the successful use of existing physics-based models and experimental data analysis: An established detailed surface reaction mechanism with associated physics-based rate parameters for a certain well-understood catalytic system consisting of an active catalyst material (PdO) and support material (Al_2O_3) serves as the basis for the establishment of new sets of kinetic data for a similar catalytic system, here PdO as the active material with different supports, i.e., SnO_2 and ZrO_2. The derivation of the new kinetic schemes uses a numerical algorithm for optimizing the kinetic parameters in order to fit experimental observations for each of the different supported catalysts. This procedure substantially accelerates model development for catalytic systems, for which a detailed "role model" already exists; however, minor changes are mandatory. Nevertheless, this procedure can only be applied if the catalyst modification, such as the use of a different support, does not lead to a new reaction mechanism network. Commonly, the development of technical catalysts relies on a single active material, while its activity is improved by varying the support and synthesis procedures without changing the general mechanism. Here, the proposed optimization procedure can speed up model development by orders of magnitude and support reaction engineering as well as scale-up processes.

■ ASSOCIATED CONTENT

Supporting Information

The Supporting Information is available free of charge at https://pubs.acs.org/doi/10.1021/acscatal.5c00516.

Details regarding experimental procedure, sample characterization data, and modeling procedure and equations; surface coverages of species and reaction preference data under dry and humid conditions for the PdO/ZrO_2 catalyst; detailed analysis of the energy changes in the optimized models (PDF)

■ AUTHOR INFORMATION

Corresponding Author

Olaf Deutschmann − *Institute for Chemical Technology and Polymer Chemistry (ITCP), Karlsruhe Institute of Technology (KIT), Karlsruhe 76131, Germany; Institute of Catalysis Research and Technology (IKFT), Karlsruhe Institute of Technology (KIT), Eggenstein-Leopoldshafen 76344, Germany;* orcid.org/0000-0001-9211-7529; Email: deutschmann@kit.edu

Authors

Rinu Chacko − *Institute for Chemical Technology and Polymer Chemistry (ITCP), Karlsruhe Institute of Technology (KIT), Karlsruhe 76131, Germany*

Kevin Keller − *Institute for Chemical Technology and Polymer Chemistry (ITCP), Karlsruhe Institute of Technology (KIT), Karlsruhe 76131, Germany*

Akash B. Shirsath − *Institute for Chemical Technology and Polymer Chemistry (ITCP), Karlsruhe Institute of Technology (KIT), Karlsruhe 76131, Germany*

Sofia Angeli − *Institute of Catalysis Research and Technology (IKFT), Karlsruhe Institute of Technology (KIT), Eggenstein-Leopoldshafen 76344, Germany;* orcid.org/0000-0001-8623-047X

Patrick Lott − *Institute for Chemical Technology and Polymer Chemistry (ITCP), Karlsruhe Institute of Technology (KIT), Karlsruhe 76131, Germany;* orcid.org/0000-0001-8683-2155

Complete contact information is available at: https://pubs.acs.org/10.1021/acscatal.5c00516

Author Contributions

#R.C. and K.K. contributed equally. The manuscript was written through contributions of all authors. All authors have given approval to the final version of the manuscript.

Notes

The authors declare no competing financial interest.

■ ACKNOWLEDGMENTS

Funded by the Deutsche Forschungsgemeinschaft (DFG, German Research Foundation) − CRC-1441 − Project ID 426888090. Additionally, the authors thank S. Tischer for his expertise in DETCHEM simulations, T. Bergfeldt (IAM-AWP, KIT) for the elemental analysis, H. Störmer (LEM, KIT) for the TEM measurements, and D. Hodonj for fruitful discussions.

■ REFERENCES

(1) Gélin, P.; Primet, M. Complete Oxidation of Methane at Low Temperature over Noble Metal Based Catalysts: A Review. *Appl. Catal., B* **2002**, *39* (1), 1−37.

(2) Ciuparu, D.; Lyubovsky, M. R.; Altman, E.; Pfefferle, L. D.; Datye, A. Catalytic Combustion of Methane over Palladium-Based Catalysts. *Catal. Rev.* **2002**, *44* (4), 593−649.

(3) Howarth, R. W. A Bridge to Nowhere: Methane Emissions and the Greenhouse Gas Footprint of Natural Gas. *Energy Sci. Eng.* **2014**, *2* (2), 47−60.

(4) Liu, Z.-P.; Hu, P. General Rules for Predicting Where a Catalytic Reaction Should Occur on Metal Surfaces: A Density Functional Theory Study of C− H and C− O Bond Breaking/Making on Flat, Stepped, and Kinked Metal Surfaces. *J. Am. Chem. Soc.* **2003**, *125* (7), 1958−1967.

(5) Burch, R.; Urbano, F. J. Investigation of the Active State of Supported Palladium Catalysts in the Combustion of Methane. *Appl. Catal., A* **1995**, *124* (1), 121−138.

(6) Kikuchi, R.; Maeda, S.; Sasaki, K.; Wennerström, S.; Eguchi, K. Low-Temperature Methane Oxidation over Oxide-Supported Pd Catalysts: Inhibitory Effect of Water Vapor. *Appl. Catal., A* **2002**, *232* (1), 23−28.

(7) Alyani, M.; Smith, K. J. Kinetic Analysis of the Inhibition of CH4 Oxidation by H2O on PdO/Al2O3 and CeO2 /PdO/Al2O3 Catalysts. *Ind. Eng. Chem. Res.* **2016**, *55* (30), 8309−8318.

(8) Gholami, R.; Alyani, M.; Smith, K. J. Deactivation of Pd Catalysts by Water during Low Temperature Methane Oxidation Relevant to Natural Gas Vehicle Converters. *Catalysts* **2015**, *5* (2), 561−594.

(9) Keller, K.; Lott, P.; Stotz, H.; Maier, L.; Deutschmann, O. Microkinetic Modeling of the Oxidation of Methane Over PdO Catalysts—Towards a Better Understanding of the Water Inhibition Effect. *Catalysts* **2020**, *10* (8), 922.

(10) Gremminger, A. T.; de Carvalho, H. W. P.; Popescu, R.; Grunwaldt, J.-D.; Deutschmann, O. Influence of Gas Composition on

Activity and Durability of Bimetallic Pd-Pt/Al2O3 Catalysts for Total Oxidation of Methane. *Catal. Today* **2015**, *258*, 470−480.
(11) Chen, H.-Y.; Lugo-Jose, Y.; Fedeyko, J. M.; Toops, T. J.; Fidler, J. Irreversible Catalyst Deactivation Mechanisms of PdO/γ-Al2O3 Catalysts for Lean Methane Oxidation. *ACS Catal.* **2024**, *14* (20), 15751−15763.
(12) Karion, A.; Sweeney, C.; Pétron, G.; Frost, G.; Michael Hardesty, R.; Kofler, J.; Miller, B. R.; Newberger, T.; Wolter, S.; Banta, R.; et al. Methane Emissions Estimate from Airborne Measurements over a Western United States Natural Gas Field. *Geophys. Res. Lett.* **2013**, *40* (16), 4393−4397.
(13) Deutschmann, O.; Grunwaldt, J.-D. Abgasnachbehandlung in Mobilen Systemen: Stand Der Technik, Herausforderungen Und Perspektiven. *Chem. Ing. Technol.* **2013**, *85* (5), 595−617.
(14) Lott, P.; Casapu, M.; Grunwaldt, J.-D.; Deutschmann, O. A Review on Exhaust Gas After-Treatment of Lean-Burn Natural Gas Engines − From Fundamentals to Application. *Appl. Catal., B* **2024**, *340*, 123241.
(15) Lapisardi, G.; Urfels, L.; Gélin, P.; Primet, M.; Kaddouri, A.; Garbowski, E.; Toppi, S.; Tena, E. Superior Catalytic Behaviour of Pt-Doped Pd Catalysts in the Complete Oxidation of Methane at Low Temperature. *Catal. Today* **2006**, *117* (4), 564−568.
(16) Castellazzi, P.; Groppi, G.; Forzatti, P. Effect of Pt/Pd Ratio on Catalytic Activity and Redox Behavior of Bimetallic Pt−Pd/Al2O3 Catalysts for CH4 Combustion. *Appl. Catal., B* **2010**, *95* (3), 303−311.
(17) Narui, K.; Yata, H.; Furuta, K.; Nishida, A.; Kohtoku, Y.; Matsuzaki, T. Effects of Addition of Pt to PdO/Al2O3 Catalyst on Catalytic Activity for Methane Combustion and TEM Observations of Supported Particles. *Appl. Catal., A* **1999**, *179* (1−2), 165−173.
(18) Colussi, S.; Trovarelli, A.; Groppi, G.; Llorca, J. The Effect of CeO2 on the Dynamics of Pd−PdO Transformation over Pd/Al2O3 Combustion Catalysts. *Catal. Commun.* **2007**, *8* (8), 1263−1266.
(19) Keller, K.; Lott, P.; Tischer, S.; Casapu, M.; Grunwaldt, J.-D.; Deutschmann, O. Methane Oxidation over PdO: Towards a Better Understanding of the Influence of the Support Material. *ChemCatchem* **2023**, *15* (11), No. e202300366.
(20) Lee, J.; Lim, T. H.; Lee, E.; Kim, D. H. Promoting the Methane Oxidation on Pd/CeO2 Catalyst by Increasing the Surface Oxygen Mobility via Defect Engineering. *ChemCatchem* **2021**, *13* (16), 3706−3712.
(21) Mao, X.; Foucher, A.; Stach, E. A.; Gorte, R. J. A Study of Support Effects for CH4 and CO Oxidation over Pd Catalysts on ALD-Modified Al2O3. *Catal. Lett.* **2019**, *149*, 905−915.
(22) Keller, K.; Hodonj, D.; Zeh, L.; Caulfield, L.; Sauter, E.; Wöll, C.; Deutschmann, O.; Lott, P. Spatiotemporal Insights into Forced Dynamic Reactor Operation for Fast Light-off of Pd-Based Methane Oxidation Catalysts. *Catal. Sci. Technol.* **2024**, *14* (15), 4142−4153.
(23) Stakheev, A. Y.; Batkin, A. M.; Teleguina, N. S.; Bragina, G. O.; Zaikovsky, V. I.; Prosvirin, I. P.; Khudorozhkov, A. K.; Bukhtiyarov, V. I. Particle Size Effect on CH4 Oxidation over Noble Metals: Comparison of Pt and Pd Catalysts. *Top. Catal.* **2013**, *56*, 306−310.
(24) Chin, Y.-H.; García-Diéguez, M.; Iglesia, E. Dynamics and Thermodynamics of Pd−PdO Phase Transitions: Effects of Pd Cluster Size and Kinetic Implications for Catalytic Methane Combustion. *J. Phys. Chem. C* **2016**, *120* (3), 1446−1460.
(25) Ciuparu, D.; Perkins, E.; Pfefferle, L. In Situ DR-FTIR Investigation of Surface Hydroxyls on γ-Al 2O3 Supported PdO Catalysts during Methane Combustion. *Appl. Catal., A* **2004**, *263* (2), 145−153.
(26) Ciuparu, D.; Bozon-Verduraz, F.; Pfefferle, L. Oxygen Exchange between Palladium and Oxide Supports in Combustion Catalysts. *J. Phys. Chem. B* **2002**, *106* (13), 3434−3442.
(27) Roth, D.; Gélin, P.; Primet, M.; Tena, E. Catalytic Behaviour of Cl-Free and Cl-Containing Pd/Al2O3 Catalysts in the Total Oxidation of Methane at Low Temperature. *Appl. Catal., A* **2000**, *203* (1), 37−45.
(28) Burch, R. Low NOx Options in Catalytic Combustion and Emission Control. *Catal. Today* **1997**, *35* (1), 27−36.
(29) Velin, P.; Hemmingsson, F.; Schaefer, A.; Skoglundh, M.; Lomachenko, K. A.; Raj, A.; Thompsett, D.; Smedler, G.; Carlsson, P.-A. Hampered PdO Redox Dynamics by Water Suppresses Lean Methane Oxidation over Realistic Palladium Catalysts. *ChemCatchem* **2021**, *13* (17), 3765−3771.
(30) Schwartz, W. R.; Pfefferle, L. D. Combustion of Methane over Palladium-Based Catalysts: Support Interactions. *J. Phys. Chem. C* **2012**, *116* (15), 8571−8578.
(31) Schwartz, W. R.; Ciuparu, D.; Pfefferle, L. D. Combustion of Methane over Palladium-Based Catalysts: Catalytic Deactivation and Role of the Support. *J. Phys. Chem. C* **2012**, *116* (15), 8587−8593.
(32) Gao, D.; Zhang, C.; Wang, S.; Yuan, Z.; Wang, S. Catalytic Activity of Pd/Al2O3 toward the Combustion of Methane. *Catal. Commun.* **2008**, *9* (15), 2583−2587.
(33) Gigola, C. E.; Moreno, M. S.; Costilla, I.; Sanchez, M. D. Characterization of Pd−CeOx Interaction on α-Al2O3 Support. *Appl. Surf. Sci.* **2007**, *254* (1), 325−329.
(34) Fuentes, R. O.; Acuña, L. M.; Leyva, A. G.; Baker, R. T.; Pan, H.; Chen, X.; Delgado-Jaén, J. J. Physicochemical Properties of Nanostructured Pd/Lanthanide-Doped Ceria Spheres with High Catalytic Activity for CH4 Combustion. *J. Mater. Chem. A* **2018**, *6* (17), 7488−7499.
(35) Kaya, D.; Singh, D.; Kincal, S.; Uner, D. Facilitating Role of Pd for Hydrogen, Oxygen and Water Adsorption/Desorption Processes from Bulk CeO2 and CeO2/γ-Al2O3. *Catal. Today* **2019**, *323*, 141−147.
(36) Lott, P.; Dolcet, P.; Casapu, M.; Grunwaldt, J. D.; Deutschmann, O. The Effect of Prereduction on the Performance of Pd/Al2o3 and Pd/Ceo2 Catalysts during Methane Oxidation. *Ind. Eng. Chem. Res.* **2019**, *58* (28), 12561−12570.
(37) Kolaczkowski, S. T.; Thomas, W. J.; Titiloye, J.; Worth, D. J. Catalytic Combustion of Methane in a Monolith Reactor: Heat and Mass Transfer under Laminar Flow and Pseudo-Steady-State Reaction Conditions. *Combust. Sci. Technol.* **1996**, *118* (1−3), 79−100.
(38) Hayes, R. E.; Kolaczkowski, S. T.; Li, P. K. C.; Awdry, S. The Palladium Catalysed Oxidation of Methane: Reaction Kinetics and the Effect of Diffusion Barriers. *Chem. Eng. Sci.* **2001**, *56* (16), 4815−4835.
(39) Torkashvand, H.; Gremminger, A.; Valchera, S.; Casapu, M.; Grunwaldt, J.-D.; Deutschmann, O. The Impact of Pre-Turbine Catalyst Placement on Methane Oxidation in Lean-Burn Gas Engines: An Experimental and Numerical Study. *SAE Technol. Pap.* **2017**, *2017*, 01.
(40) Wang, M.; Chen, H.-Y.; Lugo-Jose, Y.; Fedeyko, J. M.; Toops, T. J.; Fidler, J. Mechanistic and Kinetic Analysis of Complete Methane Oxidation on a Practical PtPd/Al2O3 Catalyst. *Catalysts* **2024**, *14*, 847.
(41) Schmider, D.; Maier, L.; Deutschmann, O. Reaction Kinetics of CO and CO2Methanation over Nickel. *Ind. Eng. Chem. Res.* **2021**, *60* (16), 5792−5805.
(42) Stotz, H.; Maier, L.; Boubnov, A.; Gremminger, A. T.; Grunwaldt, J. D.; Deutschmann, O. Surface Reaction Kinetics of Methane Oxidation over PdO. *J. Catal.* **2019**, *370*, 152−175.
(43) den Bossche, M. V.; Grönbeck, H. Methane Oxidation over PdO(101) Revealed by First-Principles Kinetic Modeling. *J. Am. Chem. Soc.* **2015**, *137* (37), 12035−12044.
(44) Bruix, A.; Margraf, J. T.; Andersen, M.; Reuter, K. First-Principles-Based Multiscale Modelling of Heterogeneous Catalysis. *Nat. Catal.* **2019**, *2* (8), 659−670.
(45) Wellendorff, J.; Silbaugh, T. L.; Garcia-Pintos, D.; Nørskov, J. K.; Bligaard, T.; Studt, F.; Campbell, C. T. A Benchmark Database for Adsorption Bond Energies to Transition Metal Surfaces and Comparison to Selected DFT Functionals. *Surf. Sci.* **2015**, *640*, 36−44.
(46) Matera, S.; Schneider, W. F.; Heyden, A.; Savara, A. Progress in Accurate Chemical Kinetic Modeling, Simulations, and Parameter Estimation for Heterogeneous Catalysis. *ACS Catal.* **2019**, *9* (8), 6624−6647.

https://doi.org/10.1021/acscatal.5c00516
ACS Catal. 2025, 15, 6937−6952

(47) Medford, A. J.; Wellendorff, J.; Vojvodic, A.; Studt, F.; Abild-Pedersen, F.; Jacobsen, K. W.; Bligaard, T.; Nørskov, J. K. Assessing the Reliability of Calculated Catalytic Ammonia Synthesis Rates. *Science* **2014**, *345* (6193), 197−200.
(48) Kreitz, B.; Lott, P.; Studt, F.; Medford, A. J.; Deutschmann, O.; Goldsmith, C. F. Automated Generation of Microkinetics for Heterogeneously Catalyzed Reactions Considering Correlated Uncertainties. *Angew. Chem., Int. Ed.* **2023**, *62* (39), No. e202306514.
(49) Sutton, J. E.; Guo, W.; Katsoulakis, M. A.; Vlachos, D. G. Effects of Correlated Parameters and Uncertainty in Electronic-Structure-Based Chemical Kinetic Modelling. *Nat. Chem.* **2016**, *8* (4), 331.
(50) Kreitz, B.; Lott, P.; Bae, J.; Blöndal, K.; Angeli, S.; Ulissi, Z. W.; Studt, F.; Goldsmith, C. F.; Deutschmann, O. Detailed Microkinetics for the Oxidation of Exhaust Gas Emissions through Automated Mechanism Generation. *ACS Catal.* **2022**, *12* (18), 11137−11151.
(51) Gao, C. W.; Allen, J. W.; Green, W. H.; West, R. H. Reaction Mechanism Generator: Automatic Construction of Chemical Kinetic Mechanisms. *Comput. Phys. Commun.* **2016**, *203*, 212−225.
(52) Trovarelli, A. Catalytic Properties of Ceria and CeO2-Containing Materials. *Catal. Rev.* **1996**, *38* (4), 439−520.
(53) Murata, K.; Kosuge, D.; Ohyama, J.; Mahara, Y.; Yamamoto, Y.; Arai, S.; Satsuma, A. Exploiting Metal−Support Interactions to Tune the Redox Properties of Supported Pd Catalysts for Methane Combustion. *ACS Catal.* **2020**, *10* (2), 1381−1387.
(54) Chen, S.; Li, S.; You, R.; Guo, Z.; Wang, F.; Li, G.; Yuan, W.; Zhu, B.; Gao, Y.; Zhang, Z. Elucidation of Active Sites for CH4 Catalytic Oxidation over Pd/CeO2 via Tailoring Metal−Support Interactions. *ACS Catal.* **2021**, *11* (9), 5666−5677.
(55) Widjaja, H.; Sekizawa, K.; Eguchi, K. Low-Temperature Oxidation of Methane over Pd Supported on SnO2-Based Oxides. *Bull. Chem. Soc. Jpn.* **1999**, *72* (2), 313−320.
(56) Yu, J.; Zhao, D.; Xu, X.; Wang, X.; Zhang, N. Study on RuO2/SnO2: Novel and Active Catalysts for CO and CH4 Oxidation. *ChemCatchem* **2012**, *4* (8), 1122−1132.
(57) Sekizawa, K.; Widjaja, H.; Maeda, S.; Ozawa, Y.; Eguchi, K. Low Temperature Oxidation of Methane over Pd/SnO2 Catalyst. *Appl. Catal., A* **2000**, *200* (1−2), 211−217.
(58) Barrett, W.; Shen, J.; Hu, Y.; Hayes, R. E.; Scott, R. W. J.; Semagina, N. Understanding the Role of SnO2 Support in Water-Tolerant Methane Combustion: In Situ Observation of Pd(OH)2 and Comparison with Pd/Al2O3. *ChemCatchem* **2020**, *12* (3), 944−952.
(59) Chen, C.; Yeh, Y.-H.; Cargnello, M.; Murray, C. B.; Fornasiero, P.; Gorte, R. J. Methane Oxidation on Pd@ZrO2/Si−Al2O3 Is Enhanced by Surface Reduction of ZrO2. *ACS Catal.* **2014**, *4* (11), 3902−3909.
(60) Willis, J. J.; Gallo, A.; Sokaras, D.; Aljama, H.; Nowak, S. H.; Goodman, E. D.; Wu, L.; Tassone, C. J.; Jaramillo, T. F.; Abild-Pedersen, F. Systematic Structure−Property Relationship Studies in Palladium-Catalyzed Methane Complete Combustion. *ACS Catal.* **2017**, *7* (11), 7810−7821.
(61) Chacko, R.; Keller, K.; Tischer, S.; Shirsath, A. B.; Lott, P.; Angeli, S.; Deutschmann, O. Automating the Optimization of Catalytic Reaction Mechanism Parameters Using Basin-Hopping: A Proof of Concept. *J. Phys. Chem. C* **2023**, *127* (16), 7628−7639.
(62) Kreitz, B.; Wehinger, G. D.; Goldsmith, C. F.; Turek, T. Microkinetic Modeling of the Transient CO2Methanation with DFT-Based Uncertainties in a Berty Reactor. *ChemCatchem* **2022**, *14* (18), No. e202200570.
(63) Savara, A.; Walker, E. A. CheKiPEUQ Intro 1: Bayesian Parameter Estimation Considering Uncertainty or Error from Both Experiments and Theory. *ChemCatchem* **2020**, *12* (21), 5385−5400.
(64) Rangarajan, S.; Maravelias, C. T.; Mavrikakis, M. Sequential-Optimization-Based Framework for Robust Modeling and Design of Heterogeneous Catalytic Systems. *J. Phys. Chem. C* **2017**, *121* (46), 25847−25863.
(65) Epling, W. S.; Hoflund, G. B. Catalytic Oxidation of Methane over ZrO2-Supported Pd Catalysts. *J. Catal.* **1999**, *182* (1), 5−12.
(66) Müller, C. A.; Maciejewski, M.; Koeppel, R. A.; Baiker, A. Combustion of Methane over Palladium/Zirconia: Effect of Pd-Particle Size and Role of Lattice Oxygen. *Catal. Today* **1999**, *47* (1−4), 245−252.
(67) Grunwaldt, J.-D.; van Vegten, N.; Baiker, A. Insight into the Structure of Supported Palladium Catalysts during the Total Oxidation of Methane. *Chem. Commun.* **2007**, 4635−4637.
(68) Murata, K.; Mahara, Y.; Ohyama, J.; Yamamoto, Y.; Arai, S.; Satsuma, A. The Metal−Support Interaction Concerning the Particle Size Effect of Pd/Al2O3 on Methane Combustion. *Angew. Chem., Int. Ed.* **2017**, *129* (50), 16209−16213.

https://doi.org/10.1021/acscatal.5c00516
ACS Catal. 2025, 15, 6937−6952